AIMS Mathematics, 11(4): 12011–12042.
DOI:10.3934/math.2026493
Received: 06 February 2026
Revised: 22 March 2026
Accepted: 30 March 2026
Published: 29 April 2026

https://www.aimspress.com/journal/Math

Research article

A neural network framework for simulating drought impacts on predator–prey dynamics

Nouf Abdulrahman Alqahtani and Mohammadi Begum Jeelani*

Department of Mathematics and Statistics College of Science, Imam Mohammad Ibn Saud Islamic University (IMSIU), Riyadh, Saudi Arabia

* **Correspondence:** Email: mbshaikh@imamu.edu.sa; Tel: +966537369980.

Abstract: This study examines the influence of drought on predator–prey systems under the variable-order (VO) fractional derivative. It is applied to the wildebeest–lion system of the Serengeti. First, the well-posedness of the system is ensured by the existence, uniqueness, and Ulam–Hyers (UH) stability of the solution. A finite difference method is presented, coupled with a neural network (NN) approach for numerical validation. The numerical results show the effect of the VO fractional derivative and the intensity of the drought. The results demonstrate that a critical drought threshold exists for the drought impact parameter γ, beyond which the healthy prey populations decline by over 90% from 6643 when γ is 0.20 to 407 when γ is 0.40, and the risk of extinction is very high. As the fractional order decreases from 0.5, the ecological memory is increased, resulting in increased predator populations (from 4898 to 8974 when γ is 0.1) and the long-term effects of the drought. The VO framework produces qualitatively different dynamics than constant-order models, featuring time-dependent stability and attractor morphing, which makes it more suitable for modelling real-world ecological systems under climate stress. The NN approach also demonstrates excellent predictive capabilities, achieving $R^2 = 1.0$ and RMSE < 12 for all populations. These metrics validate our numerical scheme and provide a computationally efficient quick scenario analysis. The novelty of our analysis is the combination of a VO operator, finite difference method, and neural computing in a unified framework for analyzing nonlinear fractional ecological systems. This study provides a mathematically sound framework for understanding drought-induced population shifts and offers practical computational tools for ecological forecasting under climate change.

Keywords: predator-prey model; drought effects; variable fractional order; finite difference scheme; neural networks
Mathematics Subject Classification: 03C65, 26A33, 34A08, 92B20

1. Introduction

Fractional calculus has emerged as a transformative framework in applied mathematics and theoretical biology for modelling systems with anomalous dynamics that lie beyond the scope of conventional models [1]. In contrast to classical derivatives that are local in nature, fractional derivatives include memory and hereditary properties. The past states influence current dynamics in a mathematically tractable way. This nonlocal property of fractional calculus finds a significant application in ecological systems where population growth depends on accumulated resource availability, reproduction rate depends on past nutritional levels, predator–prey interactions are influenced by memory effects in learning and habituation processes, and drought processes have a legacy effect that lasts over a season.

The variable-order derivative (VOD) extends the fractional calculus framework to include a varying memory strength over time [2]. This is a significant extension because memory effects are more pronounced during and after a drought process, memory decays at different rates depending on seasonal conditions, and past versus current conditions vary as ecosystems adapt to changing conditions. Our VOD formulation incorporates these effects more realistically to represent a drought process.

Mathematical modelling has become indispensable for understanding complex ecological and epidemiological dynamics. In predator–prey systems, significant progress has been made in incorporating realistic biological factors such as Allee effects, fear effects, and nonlocal competition. A Filippov great tit–gypsy moth model with double Allee effects and threshold control strategies has been analyzed in [3]. Bifurcation phenomena in modified Leslie–Gower models incorporating nonlocal competition and fear effects have been investigated in [4, 5]. Spatial patterns and Turing bifurcations have also been extensively studied. For instance, a study in [6] has examined Turing patterns in predator–prey systems with double Allee effects, and work in [7] has explored spatially inhomogeneous periodic solutions induced by nonlocal competition. More recently, contributions to understanding Turing–Hopf bifurcations, threshold dynamics in disease transmission, and finite-time attractivity in epidemic systems have been made in [8–10].

In parallel, fractional-order modelling has gained popularity for capturing memory and hereditary properties in biological systems. Foundational numerical methods for fractional-order biological systems have been provided in [11], and fractional calculus has been applied to model Salmonella bacterial infection with memory effects in [12]. More recently, the importance of threshold dynamics and delayed responses in ash infectious disease models has been demonstrated in [13], highlighting the need for time-dependent mechanisms.

Over recent decades, climate change has emerged as one of the major disturbances to biological systems, with drought viewed as a key factor [14]. Drought, which refers to an extended period of low water availability, affects vegetation and the landscape in various ways, which consequently affects the dynamics of the food chain. Recent mathematical models have been used to investigate the effects of drought on predator and prey dynamics, with specific reference to the effects of migration on the behavior of the predators [15]. For example, drought affects the 'landscape of fear' in the African savannas for grazing herbivores, which consequently affects their response to predation [16]. Climate factors affecting the susceptibility of prey have been established to have a significant effect on predation dynamics, ranging from short-term cycles to long-term cycles [17]. The effects of seasonal changes, including drought, on the dynamics of predation and prey have been discussed at length using

mathematical models [18].

Despite this, the existing fractional models mostly use derivatives of constant order. In the existing fractional models, the memory strength is assumed to be fixed. However, the memory strength is expected to change when modelling ecological systems under extreme climate conditions. Therefore, the present work addresses the gap in the existing literature by developing a new mathematical framework using VO fractional derivatives.

However, the incorporation of climate stressors like drought into fractional VO modelling remains an underexplored area. Drought can be considered a unique perturbation that impacts prey vulnerability and habitat quality and can even influence prey migration patterns. Our VO fractional calculus modelling approach can be effectively used to model drought effects because environmental stress effects are memory-dependent; that is, the effect of drought at any given time t depends on past levels of drought exposure.

Our study offers several important contributions. First, we provide a complete qualitative analysis, including the existence, uniqueness, and Ulam–Hyers (UH) stability of the solutions. Second, a finite difference scheme is developed for the approximate solution of the specified problem. Finally, we employ a neural network (NN) to improve the accuracy of the numerical solution, subjecting the model to thorough scalability and robustness analysis to validate its performance. These results and techniques are important, as they provide an effective approach to predict the complex and memory-dependent effects of drought on predator–prey systems.

The rest of the paper is outlined as follows. In Section 2, the formulation of the model, assumptions, and definitions are provided. In Section 3, the qualitative analysis of the fractional VO predator–prey system is presented. In Section 4, the UH stability analysis is provided. In Section 5, the numerical method is presented along with the results and discussion. In Section 6, the NN method is presented. Section 7 provides scalability and robustness analysis. In Section 8, the conclusion of the work is presented.

2. Model formulation

The following is a classical continuous predator–prey system that incorporates the concept of drought and is parameterized for the Serengeti wildebeest–lion ecosystem:

$$\begin{cases} D_t\mathcal{N}_1 = r\mathcal{N}_1\left(1-\dfrac{\mathcal{N}_1}{K}\right) - \dfrac{a_0\mathcal{N}_1\mathcal{P}}{1+b\mathcal{N}_1} - \gamma\mathcal{N}_1 - \mu_0\mathcal{N}_1 + b_1\mathcal{N}_2, \\ D_t\mathcal{N}_2 = \gamma\mathcal{N}_1 - a_1\mathcal{N}_2\mathcal{P} - \mu_0\mathcal{N}_2 - \sigma\mathcal{N}_2 - b_1\mathcal{N}_2, \\ D_t\mathcal{P} = \dfrac{\beta_1 a_0\mathcal{N}_1\mathcal{P}}{1+b\mathcal{N}_1} + \beta_2 a_1\mathcal{N}_2\mathcal{P} - \mu_1\mathcal{P}, \\ \mathcal{N}_1(0) = \mathcal{N}_{10}, \quad \mathcal{N}_2(0) = \mathcal{N}_{20}, \quad \mathcal{P}(0) = \mathcal{P}_0. \end{cases} \tag{2.1}$$

The above model (2.1) is presented in the form of a flowchart as in Figure 1.

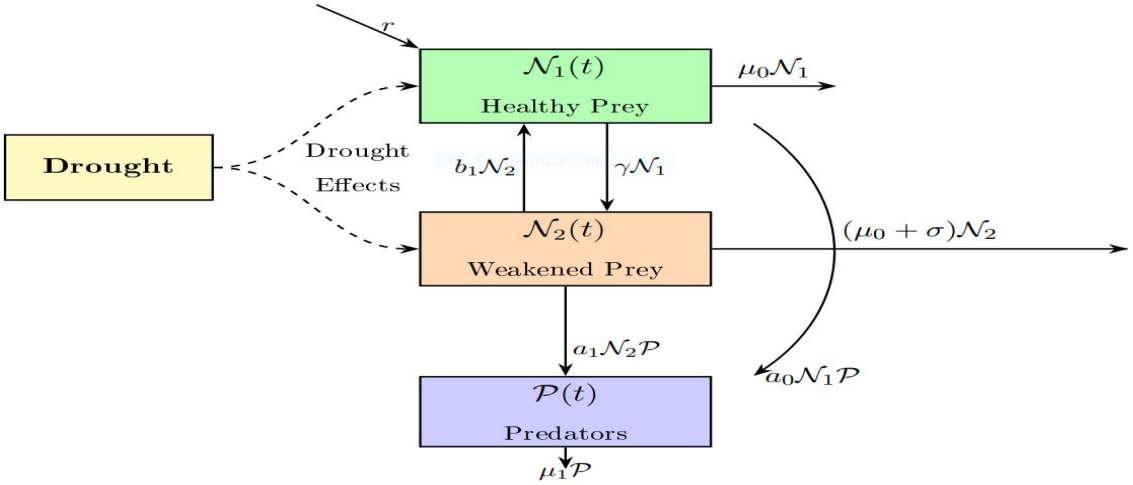

Figure 1. Schematic diagram of species-environment interactions.

The populations $\mathcal{N}_1(t)$, $\mathcal{N}_2(t)$, and $\mathcal{P}(t)$ represent healthy wildebeest, drought-weakened wildebeest, and lions at time t, respectively. The healthy prey exhibits logistic growth constrained by environmental carrying capacity K. Recruitment of susceptible healthy prey occurs at rate r. Natural mortality removes individuals from $\mathcal{N}_1(t)$ at rate μ_0, and predation affects this compartment at rate a_0. Drought-exposed individuals from $\mathcal{N}_1(t)$ transition to the weakened prey class $\mathcal{N}_2(t)$ at rate γ. A subset of $\mathcal{N}_2(t)$ then moves into the predator compartment $\mathcal{P}(t)$ at rate a_1. The weakened prey experience both natural mortality μ_0 and drought-induced death σ. Upon drought cessation, $\mathcal{N}_2(t)$ individuals recover and rejoin $\mathcal{N}_1(t)$ at rate b_1. The predator population $\mathcal{P}(t)$ is subject to natural mortality at rate μ_1.

Table 1 presents the complete details of the parameters, including symbols, descriptions, numerical values with units, and references.

Table 1. Model parameters: symbols, descriptions, numerical values (units), and references.

Symbol	Description	Value [Unit]	Source
r	Per capita growth rate of prey	0.2 [month^{-1}]	[19]
K	Environmental carrying capacity	50,000 [individuals]	Estimated
a_0	Predation rate on healthy prey N_1	0.00674 [predator^{-1} month^{-1}]	[20]
b	Saturation constant	0.5 [dimensionless]	[21]
γ	Drought impact intensity	0.1–0.5 [month^{-1}]	Estimated
a_1	Predation rate on stressed prey N_2	0.00044 [predator^{-1} month^{-1}]	[21]
μ_0	Baseline prey mortality rate	0.00001 [month^{-1}]	[20]
σ	Drought-induced mortality rate on N_2	0.0125 [month^{-1}]	[19]
β_1	Conversion efficiency from N_1	0.04 [dimensionless]	[21]
β_2	Conversion efficiency from N_2	0.04 [dimensionless]	[21]
$N_1(0)$	Initial healthy prey population	10,000 [individuals]	[22]
$N_2(0)$	Initial stressed prey population	200 [individuals]	Estimated
$P(0)$	Initial predator population	60 [individuals]	[22]
μ_1	Predator natural mortality rate	0.00001 [month^{-1}]	[20]

The γ parameter, ranging from 0.1 to 0.5, controls the rate of healthy prey transitioning to weakened prey due to drought-induced stress. Biologically, this corresponds to observed phenomena where herbivores in drought conditions experience nutritional stress, reduced immune function, and increased vulnerability to predation. The σ parameter represents additional mortality rates due to drought-induced stress. This is equivalent to direct and indirect effects of drought, such as dehydration and starvation, in addition to indirect effects such as increased disease susceptibility. When $\varphi(t)$ is low, the system has a strong memory effect, and the current population dynamics are heavily affected by past drought conditions. This is equivalent to phenomena such as soil moisture depletion in ecosystems, vegetation community changes that recover slowly after a drought, and predator and prey interaction rates affected by changes in habitat and generational changes in prey body condition and reproductive potential. The combination of these three parameters—mechanisms, direct transition, increased mortality, and memory effects—provides a comprehensive representation of drought impacts that captures both immediate and long-term ecological consequences.

2.1. Model assumptions

I. The prey population exhibits logistic growth in the absence of predators. This implies the population increases or decreases exponentially until reaching a maximum sustainable limit, known as the carrying capacity.
II. The system is considered closed, meaning there is no migration into or out of the modeled environment.
III. Predators are assumed to consume only a single species of prey.
IV. The reproductive rate of the predator population is dependent on the quantity of prey biomass converted into usable energy.
V. Predation follows a Holling Type II functional response for healthy prey and a Holling Type I response for weakened prey.
VI. Only healthy prey are capable of reproduction, as weakened prey are assumed unable to support gestation.
VII. Drought is assumed to directly impact only the prey species. Predators are not directly affected but respond indirectly through changes in prey density, making this a key feature reflecting species interdependence in the ecological model.
VIII. No interspecific competition is considered within the model.

Model (2.1) is extended to the desired VO fractional model, which is given as follows:

$$\begin{cases} D_t^{\varphi(t)}\mathcal{N}_1 = r\mathcal{N}_1\left(1-\dfrac{\mathcal{N}_1}{K}\right) - \dfrac{a_0\mathcal{N}_1\mathcal{P}}{1+b\mathcal{N}_1} - \gamma\mathcal{N}_1 - \mu_0\mathcal{N}_1 + b_1\mathcal{N}_2, \\ D_t^{\varphi(t)}\mathcal{N}_2 = \gamma\mathcal{N}_1 - a_1\mathcal{N}_2\mathcal{P} - \mu_0\mathcal{N}_2 - \sigma\mathcal{N}_2 - b_1\mathcal{N}_2, \\ D_t^{\varphi(t)}\mathcal{P} = \dfrac{\beta_1 a_0\mathcal{N}_1\mathcal{P}}{1+b\mathcal{N}_1} + \beta_2 a_1\mathcal{N}_2\mathcal{P} - \mu_1\mathcal{P}, \\ \mathcal{N}_1(0) = \mathcal{N}_{10}, \quad \mathcal{N}_2(0) = \mathcal{N}_{20}, \quad \mathcal{P}(0) = \mathcal{P}_0, \end{cases} \tag{2.2}$$

where $\varphi : \mathbb{R} \to (0, 1]$ is continuous function.

We define the Banach space $\mathcal{X} = \mathcal{Y} \times \mathcal{Y} \times \mathcal{Y}$, where $\mathcal{Y} = C([0, T], \mathbb{R})$ with the following norm:

$$\|(\mathcal{N}_1, \mathcal{N}_2, \mathcal{P})\| = \max_{t\in\mathbb{I}} \left\{ |(\mathcal{N}_1(t), \mathcal{N}_2(t), \mathcal{P}(t))| \right\}, \quad \text{where } \mathbb{I} = [0, T].$$

Let $\varphi(t) > 0$ and $y \in L^1([0, T], \mathbb{R})$ be a continuous function; then, the VO integration of y is defined as

$$\mathbf{I}_t^{\varphi(t)} y(t) = \int_0^t \frac{(t-\theta)^{\varphi(t)-1}}{\Gamma(\varphi(t))} y(\theta)\, d\theta,$$

such that the integral exists. Let $y \in \mathcal{Y}$ so that VOD with order $\varphi(t)$ can be defined as

$$D_t^{\varphi(t)} y(t) = \begin{cases} \int_0^t \frac{(t-\theta)^{\omega-\varphi(t)-1}}{\Gamma(\omega-\varphi(t))} \frac{d^\omega}{d\theta^\omega} y(\theta)\, d\theta, & \omega - 1 < \varphi(t) < \omega, \\ \frac{d^\omega y}{dt^\omega}, & \varphi(t) = \omega, \end{cases}$$

where $\omega = \lceil \varphi(t) \rceil$.

$$D_t^{\varphi(t)} y(t) = \begin{cases} \int_0^t \frac{(t-\theta)^{-\varphi(t)}}{\Gamma(1-\varphi(t))} \frac{d}{d\theta} y(\theta)\, d\theta, & 0 < \varphi(t) < 1, \\ D_t y, & \varphi(t) = 1. \end{cases}$$

3. Theoretical analysis

We analyze System (2.2) theoretically in this section through the application of the Schauder and Banach fixed-point theorems. To proceed, we define the following:

$$\begin{cases} \psi_1(t, \mathcal{N}_1, \mathcal{N}_2, \mathcal{P}) = r\mathcal{N}_1 \left(1 - \frac{\mathcal{N}_1}{K}\right) - \frac{a_0 \mathcal{N}_1 \mathcal{P}}{1 + b\mathcal{N}_1} - \gamma \mathcal{N}_1 - \mu_0 \mathcal{N}_1 + b_1 \mathcal{N}_2, \\ \psi_2(t, \mathcal{N}_1, \mathcal{N}_2, \mathcal{P}) = \gamma \mathcal{N}_1 - a_1 \mathcal{N}_2 \mathcal{P} - \mu_0 \mathcal{N}_2 - \sigma \mathcal{N}_2 - b_1 \mathcal{N}_2, \\ \psi_3(t, \mathcal{N}_1, \mathcal{N}_2, \mathcal{P}) = \frac{\beta_1 a_0 \mathcal{N}_1 \mathcal{P}}{1 + b\mathcal{N}_1} + \beta_2 a_1 \mathcal{N}_2 \mathcal{P} - \mu_1 \mathcal{P}. \end{cases}$$

$$\mathcal{F}(t) = \begin{cases} \mathcal{N}_1(t) \\ \mathcal{N}_2(t) \\ \mathcal{P}(t) \end{cases}, \mathcal{F}(0) = \begin{cases} \mathcal{N}_1(0) \\ \mathcal{N}_2(0) \\ \mathcal{P}(0) \end{cases}, \Psi(t, \mathcal{F}(t)) = \begin{cases} \psi_1(t, \mathcal{N}_1, \mathcal{N}_2, \mathcal{P}) \\ \psi_2(t, \mathcal{N}_1, \mathcal{N}_2, \mathcal{P}) \\ \psi_2(t, \mathcal{N}_1, \mathcal{N}_2, \mathcal{P}) \end{cases}.$$

Hence, in light of these mentioned functions, System (2.2) can be written as:

$$\begin{cases} D_t^{\varphi} \mathcal{F}(t) = \Psi(t, \mathcal{F}(t)), \\ \mathcal{F}(0) = \mathcal{F}_0. \end{cases} \tag{3.1}$$

Lemma 1. *The solution to the initial value problem* (3.1) *can be expressed as:*

$$\mathcal{F}(t) = \mathcal{F}_0 + \int_0^t \frac{(t-\theta)^{\varphi(t)-1}}{\Gamma(\varphi(t))} \Psi(\theta, \mathcal{F}(\theta)) d\theta. \tag{3.2}$$

Consider an operator, $\mathfrak{T} : \mathcal{X} \to \mathcal{X}$ from (3.2) as given as:

$$\mathfrak{T}(\mathcal{F}(t)) = \mathcal{F}_0 + \int_0^t \frac{(t-\theta)^{\varphi(t)-1}}{\Gamma(\varphi(t))}\Psi(\theta, \mathcal{F}(\theta))d\theta. \tag{3.3}$$

The following assumptions are required to achieve the results:

(A_1) The function Ψ is continuous and satisfies the Lipschitz condition. There exists $L_\Psi > 0$ such that for all $\mathcal{F}, \bar{\mathcal{F}} \in \mathcal{X}$,

$$|\Psi(t, \mathcal{F}(t)) - \Psi(t, \bar{\mathcal{F}}(t))| \leq L_\Psi |\mathcal{F}(t) - \bar{\mathcal{F}}(t)|.$$

(A_2) Ψ is bounded. There exists $K_\Psi > 0$ such that for all $\mathcal{F} \in \mathcal{X}$,

$$|\Psi(t, \mathcal{F}(t))| \leq K_\Psi |\mathcal{F}(t)|.$$

Theorem 1. *If Assumption* (A_1) *is satisfied, and* $\Phi L_\Psi < 1$, *where* $\Phi = \max_{t\in\mathbb{I}} \left\{t^{\varphi(t)}/\Gamma(\varphi(t)+1)\right\}$, *then Problem* (3.3) *has a unique solution.*

Proof. For $\mathcal{F}, \bar{\mathcal{F}} \in \mathcal{X}$ and $t \in \mathbb{I}$, we consider

$$\begin{aligned}
\|\mathfrak{T}(\mathcal{F}) - \mathfrak{T}(\bar{\mathcal{F}})\| &= \max_{t\in\mathbb{I}} \left\{ \left| \int_0^t \frac{(t-\theta)^{\varphi(t)-1}}{\Gamma(\varphi(t))}\Psi(\theta, \mathcal{F}(\theta))d\theta - \int_0^t \frac{(t-\theta)^{\varphi(t)-1}}{\Gamma(\varphi(t))}\Psi(\theta, \bar{\mathcal{F}}(\theta))d\theta \right| \right\} \\
&= \max_{t\in\mathbb{I}} \left\{ \left| \int_0^t \frac{(\Psi(\theta, \mathcal{F}(\theta)) - \Psi(\theta, \bar{\mathcal{F}}(\theta)))}{\Gamma(\varphi(t))}(t-\theta)^{\varphi(t)-1}d\theta \right| \right\} \\
&\leq \max_{t\in\mathbb{I}} \left\{ \int_0^t \left| \frac{(\Psi(\theta, \mathcal{F}(\theta)) - \Psi(\theta, \bar{\mathcal{F}}(\theta)))(t-\theta)^{\varphi(t)-1}}{\Gamma(\varphi(t))} \right| d\theta \right\} \\
&\leq \max_{t\in\mathbb{I}} \left\{ \left| \frac{(\Psi(\theta, \mathcal{F}(\theta)) - \Psi(\theta, \bar{\mathcal{F}}(\theta)))}{\Gamma(\varphi(t))} \right| \int_0^t (t-\theta)^{\varphi(t)-1}d\theta \right\} \\
&\leq \max_{t\in\mathbb{I}} \left\{ \frac{\left|\Psi\mathcal{F}(t) - \Psi\bar{\mathcal{F}}(t)\right|}{\Gamma(\varphi(t))} \int_0^t (t-\theta)^{\varphi(t)-1}d\theta \right\} \\
&\leq \max_{t\in\mathbb{I}} \left\{ \frac{L_\Psi\, t^{\varphi(t)}|\mathcal{F}(t) - \bar{\mathcal{F}}(t)|}{\Gamma(\varphi(t)+1)} \right\} \\
&\leq \Phi L_\Psi \|\mathcal{F} - \bar{\mathcal{F}}\|.
\end{aligned}$$

Because $\Phi L_\Psi < 1$, $\mathfrak{T}$ is a contraction mapping. By the Banach fixed-point theorem, $\mathfrak{T}$ has a unique fixed point, which is the unique solution to Problem (3.3). □

Theorem 2. *If Assumptions* (A_1) *and* (A_2) *are satisfied, then Problem* (3.3) *has at least one solution.*

Proof. To apply Schauder's theorem to $\mathfrak{T} : X \to \mathcal{X}$, choose $r > 0$ such that

$$|\mathcal{F}_0| + rK_\psi\Phi \leq r,$$

and the convex subset $\mathcal{X}$ is defined by:,

$$E = \{\mathcal{F} \in \mathcal{X} : \|\mathcal{F}\| < r\}.$$

The proof proceeds according to the following steps:

Step 1:

For the continuity of $\mathfrak{T}$, consider a convergent sequence $\mathcal{F}_n \to \mathcal{F}$ in $\mathcal{X}$. We examine

$$\begin{aligned}
\|\mathfrak{T}(\mathcal{F}_n) - \mathfrak{T}(\mathcal{F})\| &= \max_{t\in\mathbb{I}} \left\{ \left| \int_0^t \frac{(t-\theta)^{\varphi(t)-1}}{\Gamma(\varphi(t))} \Psi(\theta, \mathcal{F}_n(\theta)) d\theta - \int_0^t \frac{(t-\theta)^{\varphi(t)-1}}{\Gamma(\varphi(t))} \Psi(\theta, \mathcal{F}(\theta)) d\theta \right| \right\} \\
&= \max_{t\in\mathbb{I}} \left\{ \left| \int_0^t \frac{(\Psi(\theta, \mathcal{F}_n(\theta)) - \Psi(\theta, \mathcal{F}(\theta)))}{\Gamma(\varphi(t))} (t-\theta)^{\varphi(t)-1} d\theta \right| \right\} \\
&\leq \max_{t\in\mathbb{I}} \left\{ \int_0^t \frac{\left|(\Psi(\theta, \mathcal{F}_n(\theta)) - \Psi(\theta, \mathcal{F}(\theta)))(t-\theta)^{\varphi(t)-1}\right|}{\Gamma(\varphi(t))} d\theta \right\} \\
&\leq \max_{t\in\mathbb{I}} \left\{ |\Psi\mathcal{F}_n(t) - \Psi\mathcal{F}(t)| \frac{\int_0^t (t-\theta)^{\varphi(t)-1} d\theta}{\Gamma(\varphi(t))} \right\} \\
&\leq L_\Psi \|\mathcal{F}_n - \mathcal{F}\| \max_{t\in\mathbb{I}} \left\{ \frac{t^{\varphi(t)}}{\Gamma(\varphi(t)+1)} \right\} \\
&\leq \Phi L_\Psi \|\mathcal{F}_n - \mathcal{F}\|.
\end{aligned}$$

□

Thus, $\|\mathfrak{T}(\mathcal{F}_n) - \mathfrak{T}(\mathcal{F})\| \to 0$ as $n \to \infty$; hence, $\mathfrak{T}$ is continuous on E.

Step 2:

Under the mapping $\mathfrak{T}$, the image of any bounded set remains bounded.

We must show $|\mathfrak{T}(\mathcal{F})| \leq r$ for any $\mathcal{F} \in \mathcal{X}$. Given $\mathcal{F} \in \mathcal{X}$, observe that

$$\begin{aligned}
\|\mathfrak{T}(\mathcal{F})\| &= \max_{t\in\mathbb{I}} \left| \mathcal{F}_0 + \int_0^t \frac{(t-\theta)^{\varphi(t)-1}}{\Gamma(\varphi(t))} \Psi(\theta, \mathcal{F}(\theta)) d\theta \right| \\
&\leq |\mathcal{F}_0| + \max_{t\in\mathbb{I}} \left\{ \frac{|(\Psi(\theta, \mathcal{F}(\theta))|}{\Gamma(\varphi(t))} \int_0^t (t-\theta)^{\varphi(t)-1} d\theta \right\} \\
&\leq |\mathcal{F}_0| + \|\Psi\mathcal{F}\| \max_{t\in\mathbb{I}} \left\{ \frac{\int_0^t (t-\theta)^{\varphi(t)-1} d\theta}{\Gamma(\varphi(t))} \right\} \\
&\leq |\mathcal{F}_0| + K_\psi \|\mathcal{F}\| \Phi \\
&\leq |\mathcal{F}_0| + r K_\psi \Phi \\
\|\mathfrak{T}(\mathcal{F})\| &\leq r.
\end{aligned}$$

Consequently, the image $\mathfrak{T}(E)$ forms a uniformly bounded subset of E.

Step 3:

We prove $\mathfrak{T}$ is equicontinuous on $\mathcal{X}$. Let $t_1, t_2 \in \mathbb{I}$, $t_1 < t_2$, and $\mathcal{F} \in E$ be arbitrary. Then,

$$\begin{aligned}
\|\mathfrak{T}(\mathcal{F}(t_2)) - \mathfrak{T}(\mathcal{F}(t_1))\| = \max_{t\in\mathbb{I}} \Bigg| & \frac{1}{\Gamma(\varphi(t_2))} \int_0^{t_2} (t_2-\theta)^{\varphi(t_2)-1} \Psi(\theta, \mathcal{F}(\theta)) d\theta \\
& - \frac{1}{\Gamma(\varphi(t_1))} \int_0^{t_1} (t_1-\theta)^{\varphi(t_1)-1} \Psi(\theta, \mathcal{F}(\theta)) d\theta \Bigg|
\end{aligned}$$

$$
\begin{aligned}
&= \|\Psi(\mathcal{F})\|\Big\{\Big(\frac{1}{\Gamma(\varphi(t_2))} - \frac{1}{\Gamma(\varphi(t_1))}\Big)\int_0^{t_1}\{(t_2-\theta)^{\varphi(t_2)-1} \\
&- (t_1-\theta)^{\varphi(t_1)-1}\}\,d\theta + \frac{1}{\Gamma(\varphi(t_2))}\int_{t_1}^{t_2}(t_2-\theta)^{\varphi(t_2)-1}d\theta\Big\} \\
&= \|\Psi(\mathcal{F})\|\Big\{\frac{{t_2}^{\varphi(t_2)} - 2(t_2-t_1)^{\varphi(t_2)}}{\Gamma(1+\varphi(t_2))} - \frac{{t_1}^{\varphi(t_1)}}{\Gamma(1+\varphi(t_1))}\Big\} \\
&= K_\psi\|\mathcal{F}\|\Big\{\frac{{t_2}^{\varphi(t_2)} - 2(t_2-t_1)^{\varphi(t_2)}}{\Gamma(1+\varphi(t_2))} - \frac{{t_1}^{\varphi(t_1)}}{\Gamma(1+\varphi(t_1))}\Big\} \\
&= rK_\psi\Big\{\frac{{t_2}^{\varphi(t_2)} - 2(t_2-t_1)^{\varphi(t_2)}}{\Gamma(1+\varphi(t_2))} - \frac{{t_1}^{\varphi(t_1)}}{\Gamma(1+\varphi(t_1))}\Big\}
\end{aligned}
$$

Therefore, as $t_1 \to t_2$,

$$\|\mathfrak{T}(\mathcal{F}(t_2)) - \mathfrak{T}(\mathcal{F}(t_1))\| \to 0.$$

Thus, $\mathfrak{T}$ is shown to be equicontinuous. All hypotheses of Schauder's theorem are therefore met, implying the existence of a fixed point for $\mathfrak{T}$ in E. Hence, Problem (3.3) admits at least one solution.

4. Stability analysis

Stability analysis is one of the important features of the qualitative study of dynamical systems. Establishing the stability of solutions of a system allows us to characterize the long-term behavior of the solutions. More importantly, the qualitative dynamics of the system remain invariant under bounded perturbations to initial states or parameters. Therefore, stability analysis is an essential part of our work [23]. Let Problem (3.1) be written as follows:

$$D_t^{\varphi}\mathcal{F}(t) = \Psi(t, \mathcal{F}(t)) + S(t). \tag{4.1}$$

Let $S(t)$ be a continuous function satisfying $S(t) \le \alpha$ for some constant $\alpha > 0$ and all $t \in \mathbb{I}$. The solution to Problem (4.1) is then expressed as:

$$
\begin{aligned}
\mathcal{F}(t) &= \mathcal{F}_0 + \int_0^t \left(\frac{(t-\theta)^{\varphi(t)-1}}{\Gamma(\varphi(t))}\Psi(\theta, \mathcal{F}(\theta))d\theta + S(\theta)\right) d\theta, \\
\mathcal{F}(t) &= \mathcal{F}_0 + \int_0^t \frac{(t-\theta)^{\varphi(t)-1}}{\Gamma(\varphi(t))}\Psi(\theta, \mathcal{F}(\theta))d\theta + \int_0^t \frac{(t-\theta)^{\varphi(t)-1}}{\Gamma(\varphi(t))}\, S(\theta)\, d\theta.
\end{aligned}
$$

In light of (3.3), we obtain

$$
\begin{aligned}
\mathcal{F}(t) &= \mathfrak{T}\mathcal{F}(t) + \int_0^t \frac{(t-\theta)^{\varphi(t)-1}}{\Gamma(\varphi(t))}\, S(\theta)\, d\theta \\
\|\mathcal{F} - \mathfrak{T}\mathcal{F}\| &= \max_{t\in\mathbb{I}}\left|\mathfrak{T}\mathcal{F}(t) + \int_0^t \frac{(t-\theta)^{\varphi(t)-1}}{\Gamma(\varphi(t))}\, S(\theta)\, d\theta - \mathfrak{T}\mathcal{F}(t)\right| \\
&\le \max_{t\in\mathbb{I}}\int_0^t \frac{(t-\theta)^{\varphi(t)-1}}{\Gamma(\varphi(t))}|S(\theta)|\, d\theta \\
&\le \max_{t\in\mathbb{I}}\frac{\alpha t^{\varphi(t)}}{\Gamma(\varphi(t)+1)} \\
&\le \alpha\Phi.
\end{aligned}
$$

Theorem 3. *Problem* (3.1) *is both UH and generalized UH stable under the condition:*

$$\Phi L_{\psi} < 1.$$

Proof. Suppose $\mathcal{F}(t)$ satisfies the inequality

$$\|\mathcal{F} - \mathfrak{T}\mathcal{F}\| \leq \alpha,$$

with $\mathcal{F}^{\star}(t)$ denoting the unique fixed point of $\mathfrak{T}$. Therefore,

$$\begin{aligned}\|\mathcal{F} - \mathcal{F}^{\star}\| &= \|\mathcal{F} - \mathfrak{T}\mathcal{F}^{\star}\| \\ &\leq \|\mathcal{F} - \mathfrak{T}\mathcal{F}\| + \|\mathfrak{T}\mathcal{F} - \mathfrak{T}\mathcal{F}^{\star}\| \\ &\leq \alpha + \Phi L_{\psi}\|\mathcal{F} - \mathcal{F}^{\star}\|.\end{aligned}$$

Hence, we obtain

$$\left(1 - \Phi L_{\psi}\right)\|\mathcal{F} - \mathcal{F}^{\star}\| \leq \alpha.$$

Therefore,

$$\begin{aligned}\|\mathcal{F} - \mathcal{F}^{\star}\| &\leq \frac{\alpha}{1 - \Phi L_{\psi}} \\ &\leq C\,\alpha,\end{aligned}$$

where $C = \frac{1}{1-\Phi L_{\psi}} > 0$. Thus Problem (3.1) is UH stable.

Consider $\zeta(\alpha) = \alpha$, which is nondecreasing such that $\zeta(0) = 0$. Therefore, the following is the desired condition for the generalized UH stability of Problem (3.1).

$$\|\mathcal{F} - \mathcal{F}^{\star}\| \leq C\,\zeta(\alpha).$$

□

5. Numerical scheme, simulations, and discussion

Numerical schemes are essential because they convert complex, real-world problems governed by differential equations into solvable computational steps. Providing a structured approach to approximation and discretization, these schemes enable accurate simulations of phenomena that are impossible to solve analytically. In our work, the fractional derivative is defined as

$$D_t^{\varphi(t)}y(t) = \begin{cases}\displaystyle\int_0^t \frac{(t-\theta)^{-\varphi(t)}}{\Gamma(1-\varphi(t))}\frac{d}{d\theta}y(\theta)\,d\theta, & 0 < \varphi(t) < 1, \\ \displaystyle\frac{d}{dt}y(t), & \varphi(t) = 1.\end{cases} \tag{5.1}$$

Consider the step size $\Delta t = T/N$, where $t \in \mathbb{I}$. Therefore, we have

$$t_n = n\Delta t, \quad n = 0, 1, \ldots, N.$$

Further, define:

$$\mathcal{N}_{1,n} \approx \mathcal{N}_1(t_n), \quad \mathcal{N}_{2,n} \approx \mathcal{N}_2(t_n), \quad \mathcal{P}_n \approx \mathcal{P}(t_n), \quad \varphi_n = \varphi(t_n).$$

Because for $\varphi_n = 1$, the fractional definition (5.1) in our work is reduced to the classical derivative, we develop the scheme for $0 < \varphi_n < 1$, applying Definition (5.1) at time t_n. The first compartment of System (2.2) implies

$$\frac{1}{\Gamma(1-\varphi_n)}\int_0^{t_n}(t_n-\theta)^{-\varphi_n}\frac{d}{d\theta}\mathcal{N}_1(\theta)\,d\theta = r\mathcal{N}_{1,n}\left(1-\frac{\mathcal{N}_{1,n}}{K}\right)-\frac{a_0\mathcal{N}_{1,n}\mathcal{P}_n}{1+b\mathcal{N}_{1,n}} - \gamma\mathcal{N}_{1,n}-\mu_0\mathcal{N}_{1,n}+b_1\mathcal{N}_{2,n}.$$

Multiply both sides by $\Gamma(1-\varphi_n)$:

$$\begin{aligned}\int_0^{t_n}(t_n-\theta)^{-\varphi_n}\frac{d}{d\theta}\mathcal{N}_1(\theta)\,d\theta = \Gamma(1-\varphi_n)\Big[r\mathcal{N}_{1,n}\left(1-\frac{\mathcal{N}_{1,n}}{K}\right)\\ -\frac{a_0\mathcal{N}_{1,n}\mathcal{P}_n}{1+b\mathcal{N}_{1,n}}-\gamma\mathcal{N}_{1,n}-\mu_0\mathcal{N}_{1,n}+b_1\mathcal{N}_{2,n}\Big].\end{aligned} \tag{5.2}$$

Approximate the derivative using differences:

$$\frac{d}{d\theta}\mathcal{N}_1(\theta)\approx\frac{\mathcal{N}_{1,j+1}-\mathcal{N}_{1,j}}{\Delta t},\quad \theta\in[t_j,t_{j+1}],\ j=0,\ldots,n-1.$$

Consequently,

$$\int_0^{t_n}(t_n-\theta)^{-\varphi_n}\frac{d}{d\theta}\mathcal{N}_1(\theta)\,d\theta\approx\sum_{j=0}^{n-1}\frac{\mathcal{N}_{1,j+1}-\mathcal{N}_{1,j}}{\Delta t}\int_{t_j}^{t_{j+1}}(t_n-\theta)^{-\varphi_n}\,d\theta. \tag{5.3}$$

Computation of the preceding integral term is given as:

$$\int_{t_j}^{t_{j+1}}(t_n-\theta)^{-\varphi_n}\,d\theta=\frac{(t_n-t_j)^{1-\varphi_n}-(t_n-t_{j+1})^{1-\varphi_n}}{1-\varphi_n}.$$

Further, consider $\tau = n-j$. Then $t_n - t_j = \tau\Delta t$ and $t_n - t_{j+1} = (\tau-1)\Delta t$:

$$\int_{t_j}^{t_{j+1}}(t_n-\theta)^{-\varphi_n}\,d\theta=\frac{(\Delta t)^{1-\varphi_n}}{1-\varphi_n}\left[\tau^{1-\varphi_n}-(\tau-1)^{1-\varphi_n}\right].$$

Thus, (5.3) becomes

$$\int_0^{t_n}(t_n-\theta)^{-\varphi_n}\frac{d}{d\theta}\mathcal{N}_1(\theta)\,d\theta\approx\sum_{j=0}^{n-1}\frac{\mathcal{N}_{1,j+1}-\mathcal{N}_{1,j}}{\varphi_n(1-\varphi_n)}\left[\tau^{1-\varphi_n}-(\tau-1)^{1-\varphi_n}\right]. \tag{5.4}$$

Hence, (5.2) implies

$$\begin{aligned}\sum_{j=0}^{n-1}\frac{\mathcal{N}_{1,j+1}-\mathcal{N}_{1,j}}{\varphi_n\Gamma(2-\varphi_n)}\left[\tau^{1-\varphi_n}-(\tau-1)^{1-\varphi_n}\right] = r\mathcal{N}_{1,n}\left(1-\frac{\mathcal{N}_{1,n}}{K}\right)-\frac{a_0\mathcal{N}_{1,n}\mathcal{P}_n}{1+b\mathcal{N}_{1,n}}\\ -\gamma\mathcal{N}_{1,n}-\mu_0\mathcal{N}_{1,n}+b_1\mathcal{N}_{2,n}.\end{aligned} \tag{5.5}$$

Putting the value of τ in (5.5), we have

$$\begin{aligned}
&\sum_{j=0}^{n-1}\left(\mathcal{N}_{1,j+1}-\mathcal{N}_{1,j}\right)\left[(n-j)^{1-\varphi_n}-(n-j-1)^{1-\varphi_n}\right]\\
&\quad=\varphi_n\Gamma(2-\varphi_n)\Bigg[r\mathcal{N}_{1,n}\left(1-\frac{\mathcal{N}_{1,n}}{K}\right)-\frac{a_0\mathcal{N}_{1,n}\mathcal{P}_n}{1+b\mathcal{N}_{1,n}}\\
&\qquad-\gamma\mathcal{N}_{1,n}-\mu_0\mathcal{N}_{1,n}+b_1\mathcal{N}_{2,n}\Bigg],\quad n\geq 1.
\end{aligned}\tag{5.6}$$

In light of (5.6), the final discretized scheme obtained for the System (2.2) is given as follows:

$$\begin{cases}
\displaystyle\sum_{j=0}^{n-1}\left(\mathcal{N}_{1,j+1}-\mathcal{N}_{1,j}\right)\left[(n-j)^{1-\varphi_n}-(n-j-1)^{1-\varphi_n}\right]\\
\quad=\varphi_n\Gamma(2-\varphi_n)\Bigg[r\mathcal{N}_{1,n}\left(1-\frac{\mathcal{N}_{1,n}}{K}\right)-\frac{a_0\mathcal{N}_{1,n}\mathcal{P}_n}{1+b\mathcal{N}_{1,n}}\\
\qquad-\gamma\mathcal{N}_{1,n}-\mu_0\mathcal{N}_{1,n}+b_1\mathcal{N}_{2,n}\Bigg],\\
\displaystyle\sum_{j=0}^{n-1}\left(\mathcal{N}_{2,j+1}-\mathcal{N}_{2,j}\right)\left[(n-j)^{1-\varphi_n}-(n-j-1)^{1-\varphi_n}\right]\\
\quad=\varphi_n\Gamma(2-\varphi_n)[\gamma\mathcal{N}_{1,n}-a_1\mathcal{N}_{2,n}\mathcal{P}_n\\
\qquad-\mu_0\mathcal{N}_{2,n}-\sigma\mathcal{N}_{2,n}-b_1\mathcal{N}_{2,n}],\\
\displaystyle\sum_{j=0}^{n-1}\left(\mathcal{P}_{j+1}-\mathcal{P}_j\right)\left[(n-j)^{1-\varphi_n}-(n-j-1)^{1-\varphi_n}\right]\\
\quad=\varphi_n\Gamma(2-\varphi_n)\Bigg[\frac{\beta_1 a_0\mathcal{N}_{1,n}\mathcal{P}_n}{1+b\mathcal{N}_{1,n}}\\
\qquad+\beta_2 a_1\mathcal{N}_{2,n}\mathcal{P}_n-\mu_1\mathcal{P}_n\Bigg],\quad n\geq 1.
\end{cases}\tag{5.7}$$

5.1. Numerical stability and convergence analysis

Following the approaches in [24–26], we analyze the stability and convergence properties of the proposed numerical scheme (5.7). We first introduce the following lemma:

Lemma 2. *For any* $0<\varphi_n<1$ *and* $n\geq 1$*, the coefficients*

$$\omega_j^n=(n-j)^{1-\varphi_n}-(n-j-1)^{1-\varphi_n},\quad j=0,1,\ldots,n-1$$

satisfy the following properties:

- $\omega_j^n>0$ for all $j=0,1,\ldots,n-1$;
- $\omega_0^n>\omega_1^n>\cdots>\omega_{n-1}^n$ (strictly decreasing);
- $\displaystyle\sum_{j=0}^{n-1}\omega_j^n=n^{1-\varphi_n}$;

- $\omega_{n-1}^n = 1$ for all $n \geq 1$.

Proof. The positivity follows from the monotonicity of the function $f(x) = x^{1-\varphi_n}$ (where $x = n - j$). For $0 < \varphi_n < 1$, the function $x^{1-\varphi_n}$ is strictly increasing; hence, $(n-j)^{1-\varphi_n} > (n-j-1)^{1-\varphi_n}$, proving (i). The decreasing nature of the sequence follows from the concavity of $f(x)$. Property (iii) is obtained by telescoping summation, and (iv) follows directly from the definition when $j = n - 1$. □

5.1.1. Stability analysis

We rewrite Scheme (5.7) in an equivalent form. For the first equation, we have:

$$\mathcal{N}_{1,n} = \mathcal{N}_{1,0} - \sum_{j=0}^{n-2} (\mathcal{N}_{1,j+1} - \mathcal{N}_{1,j}) \frac{\omega_{j+1}^n}{\omega_0^n} + \frac{\varphi_n \Gamma(2-\varphi_n)}{\omega_0^n} \mathcal{R}_1^n, \tag{5.8}$$

where $\mathcal{R}_1^n$ denotes the right-hand side terms:

$$\mathcal{R}_1^n = r\mathcal{N}_{1,n}\left(1 - \frac{\mathcal{N}_{1,n}}{K}\right) - \frac{a_0 \mathcal{N}_{1,n}\mathcal{P}_n}{1 + b\mathcal{N}_{1,n}} - \gamma \mathcal{N}_{1,n} - \mu_0 \mathcal{N}_{1,n} + b_1 \mathcal{N}_{2,n}.$$

Similar expressions hold for $\mathcal{N}_{2,n}$ and $\mathcal{P}_n$ with corresponding right-hand side terms $\mathcal{R}_2^n$ and $\mathcal{R}_3^n$.

Definition 1. *The numerical scheme* (5.7) *is said to be stable in the sense of Lyapunov if there exists a constant $C > 0$, independent of the step size Δt, such that for any two solutions $\mathbf{U}_n = (\mathcal{N}_{1,n}, \mathcal{N}_{2,n}, \mathcal{P}_n)$ and $\tilde{\mathbf{U}}_n = (\tilde{\mathcal{N}}_{1,n}, \tilde{\mathcal{N}}_{2,n}, \tilde{\mathcal{P}}_n)$ corresponding to different initial conditions, the following estimate holds:*

$$\|\mathbf{U}_n - \tilde{\mathbf{U}}_n\| \leq C\|\mathbf{U}_0 - \tilde{\mathbf{U}}_0\|, \quad \forall n \geq 1.$$

Theorem 4. *Assume that the VO function $\varphi(t)$ satisfies $0 < \varphi_{\min} \leq \varphi(t) \leq \varphi_{\max} < 1$ for all $t \in \mathbb{I}$ and that the right-hand side functions are Lipschitz continuous with Lipschitz constant $L > 0$. Then, the numerical scheme* (5.7) *is unconditionally stable.*

Proof. Let $\mathbf{U}_n$ and $\tilde{\mathbf{U}}_n$ be two solutions of (5.7) with initial conditions $\mathbf{U}_0$ and $\tilde{\mathbf{U}}_0$, respectively. Define the error $\mathbf{e}_n = \mathbf{U}_n - \tilde{\mathbf{U}}_n = (e_n^1, e_n^2, e_n^3)$.

From (5.8) and its analogs, we obtain for the first component:

$$\begin{aligned} e_n^1 = e_0^1 &- \sum_{j=0}^{n-2} (e_{j+1}^1 - e_j^1) \frac{\omega_{j+1}^n}{\omega_0^n} \\ &+ \frac{\varphi_n \Gamma(2-\varphi_n)}{\omega_0^n} \left(\mathcal{R}_1^n(\mathbf{U}_n) - \mathcal{R}_1^n(\tilde{\mathbf{U}}_n)\right). \end{aligned}$$

Using Lemma 2, we have $\omega_0^n = n^{1-\varphi_n} - (n-1)^{1-\varphi_n} > 0$ and $\omega_{j+1}^n/\omega_0^n \leq 1$. Moreover, the Lipschitz condition yields

$$|\mathcal{R}_1^n(\mathbf{U}_n) - \mathcal{R}_1^n(\tilde{\mathbf{U}}_n)| \leq L\|\mathbf{e}_n\|,$$

where $\|\mathbf{e}_n\| = |e_n^1| + |e_n^2| + |e_n^3|$. Taking absolute values in (5.1.1),

$$|e_n^1| \le |e_0^1| + \sum_{j=0}^{n-2}(|e_{j+1}^1| + |e_j^1|)\frac{\omega_{j+1}^n}{\omega_0^n} + \frac{\varphi_n\Gamma(2-\varphi_n)}{\omega_0^n}L\|\mathbf{e}_n\|.$$

Similar inequalities hold for $|e_n^2|$ and $|e_n^3|$. Summing these three inequalities and noting that $\omega_0^n \ge (1-\varphi_n)n^{-\varphi_n}$, we obtain

$$\|\mathbf{e}_n\| \le 3\|e_0\| + 3\sum_{j=0}^{n-2}\|\mathbf{e}_{j+1}\| + \|\mathbf{e}_j\|)\frac{\omega_{j+1}^n}{\omega_0^n} + \frac{3\varphi_n\Gamma(2-\varphi_n)}{\omega_0^n}L\|\mathbf{e}_n\|.$$

For sufficiently small Δt, we can ensure that $3\varphi_n\Gamma(2-\varphi_n)L/\omega_0^n < 1$, leading to

$$\|\mathbf{e}_n\| \le C_1\|e_0\| + C_2\sum_{j=0}^{n-2}\|\mathbf{e}_{j+1}\| + \|\mathbf{e}_j\|)\frac{\omega_{j+1}^n}{\omega_0^n},$$

where C_1 and C_2 are positive constants. Applying a discrete Grönwall-type inequality yields

$$\|\mathbf{e}_n\| \le C\|e_0\|, \quad \forall n \ge 1,$$

which completes the proof of unconditional stability. □

5.1.2. Convergence analysis

We now establish the convergence of the numerical scheme (5.7). Let $\mathcal{N}_1(t)$, $\mathcal{N}_2(t)$, and $\mathcal{P}(t)$ denote the exact solutions of System (2.2), and let $\mathcal{N}_{1,n}$, $\mathcal{N}_{2,n}$, $\mathcal{P}_n$ be the numerical approximations at $t = t_n$.

Definition 2. *Define the global errors at time t_n as:*

$$E_n^1 = \mathcal{N}_1(t_n) - \mathcal{N}_{1,n}, \quad E_n^2 = \mathcal{N}_2(t_n) - \mathcal{N}_{2,n}, \quad E_n^3 = \mathcal{P}(t_n) - \mathcal{P}_n.$$

Lemma 3. *Assume the exact solutions $\mathcal{N}_1, \mathcal{N}_2, \mathcal{P} \in C^2[0,T]$. Then, the local truncation error of scheme* (5.7) *satisfies:*

$$\|\mathbf{T}_n\| \le C_T(\Delta t)^{2-\varphi_{\max}},$$

where $\mathbf{T}_n = (T_n^1, T_n^2, T_n^3)$ is the vector of local truncation errors, and $C_T > 0$ is a constant independent of Δt.

Proof. The local truncation error for the first equation is obtained by substituting the exact solution into the numerical scheme:

$$\begin{aligned} T_n^1 = &\sum_{j=0}^{n-1}\left(\mathcal{N}_1(t_{j+1}) - \mathcal{N}_1(t_j)\right)\omega_j^n \\ &- \varphi_n\Gamma(2-\varphi_n)\left[r\mathcal{N}_1(t_n)\left(1 - \frac{\mathcal{N}_1(t_n)}{K}\right) - \frac{a_0\mathcal{N}_1(t_n)\mathcal{P}(t_n)}{1+b\mathcal{N}_1(t_n)}\right. \\ &\left. - \gamma\mathcal{N}_1(t_n) - \mu_0\mathcal{N}_1(t_n) + b_1\mathcal{N}_2(t_n)\right]. \end{aligned}$$

Using Taylor expansions around t_j and the integral representation of the fractional derivative, we obtain

$$T_n^1 = \mathcal{O}\left((\Delta t)^{2-\varphi_n}\right) \leq C_T(\Delta t)^{2-\varphi_{\max}}.$$

Similar estimates hold for T_n^2 and T_n^3, establishing the lemma. □

Theorem 5. *Under the assumptions of Lemma 3 and Theorem 4, the numerical scheme* (5.7) *converges to the exact solution with order* $2-\varphi_{\max}$. *Specifically, there exists a constant* $C > 0$, *independent of* Δt, *such that:*

$$\max_{0\leq n\leq N} \|\mathbf{E}_n\| \leq C(\Delta t)^{2-\varphi_{\max}},$$

where $\mathbf{E}_n = (E_n^1, E_n^2, E_n^3)$.

Proof. The global error satisfies the following equation derived from subtracting the numerical scheme from the exact equations:

$$\begin{aligned}\sum_{j=0}^{n-1}(E_{j+1}^1 - E_j^1)\omega_j^n = \varphi_n\Gamma(2-\varphi_n)\Bigg[r\left(\mathcal{N}_1(t_n)\left(1-\frac{\mathcal{N}_1(t_n)}{K}\right) - \mathcal{N}_{1,n}\left(1-\frac{\mathcal{N}_{1,n}}{K}\right)\right)\\ - a_0\left(\frac{\mathcal{N}_1(t_n)\mathcal{P}(t_n)}{1+b\mathcal{N}_1(t_n)} - \frac{\mathcal{N}_{1,n}\mathcal{P}_n}{1+b\mathcal{N}_{1,n}}\right)\\ - \gamma E_n^1 - \mu_0 E_n^1 + b_1 E_n^2\Bigg] + T_n^1.\end{aligned}$$

Similar equations hold for the second and third components. Using the Lipschitz continuity of the nonlinear terms and the stability result from Theorem 4, we obtain:

$$\|\mathbf{E}_n\| \leq C\sum_{k=1}^{n}\|\mathbf{T}_k\| \quad \text{for all } n \geq 1.$$

Applying Lemma 3,

$$\|\mathbf{E}_n\| \leq C\sum_{k=1}^{n} C_T(\Delta t)^{2-\varphi_{\max}} \leq CC_T N(\Delta t)^{2-\varphi_{\max}} \leq \tilde{C}(\Delta t)^{2-\varphi_{\max}-1}.$$

However, this preliminary estimate can be improved using a more refined analysis that accounts for the summation properties of the coefficients ω_j^n. Following the approach in [26], we can show that

$$\|\mathbf{E}_n\| \leq C(\Delta t)^{2-\varphi_{\max}}, \quad \forall n \leq N,$$

which establishes the desired convergence order. □

Corollary 1. *The numerical scheme* (5.7) *is consistent, stable, and convergent. Moreover, the convergence order is* $2-\varphi_{\max}$ *in the discrete* L^∞ *norm, that is*

$$\max_{0\leq n\leq N}\left(|\mathcal{N}_1(t_n) - \mathcal{N}_{1,n}| + |\mathcal{N}_2(t_n) - \mathcal{N}_{2,n}| + |\mathcal{P}(t_n) - \mathcal{P}_n|\right) = \mathcal{O}\left((\Delta t)^{2-\varphi_{\max}}\right).$$

5.2. *Simulations and discussion*

Numerical simulations of Model (2.2) are performed using the parameter values listed in Table 1. All parameters remain fixed except γ and $\varphi(t)$, which are systematically varied. The simulations use a constant step size $h = 0.05$ over a time $T = 12$ months.

Figure 2 demonstrates the population dynamics of $\mathcal{N}_1$, $\mathcal{N}_2$, and $\mathcal{P}$ for a fixed $\gamma = 0.1$ and various $\varphi(t)$ values. The curves representing $\mathcal{N}_1$, $\mathcal{N}_2$, and $\mathcal{P}$ change according to $\varphi(t)$ and then settle into a stable equilibrium. Biologically, smaller values of $\varphi(t)$ imply more intense memory effects manifesting as prolonged soil moisture deficits across seasons, delayed vegetation recovery, and cumulative nutritional stress in prey populations.

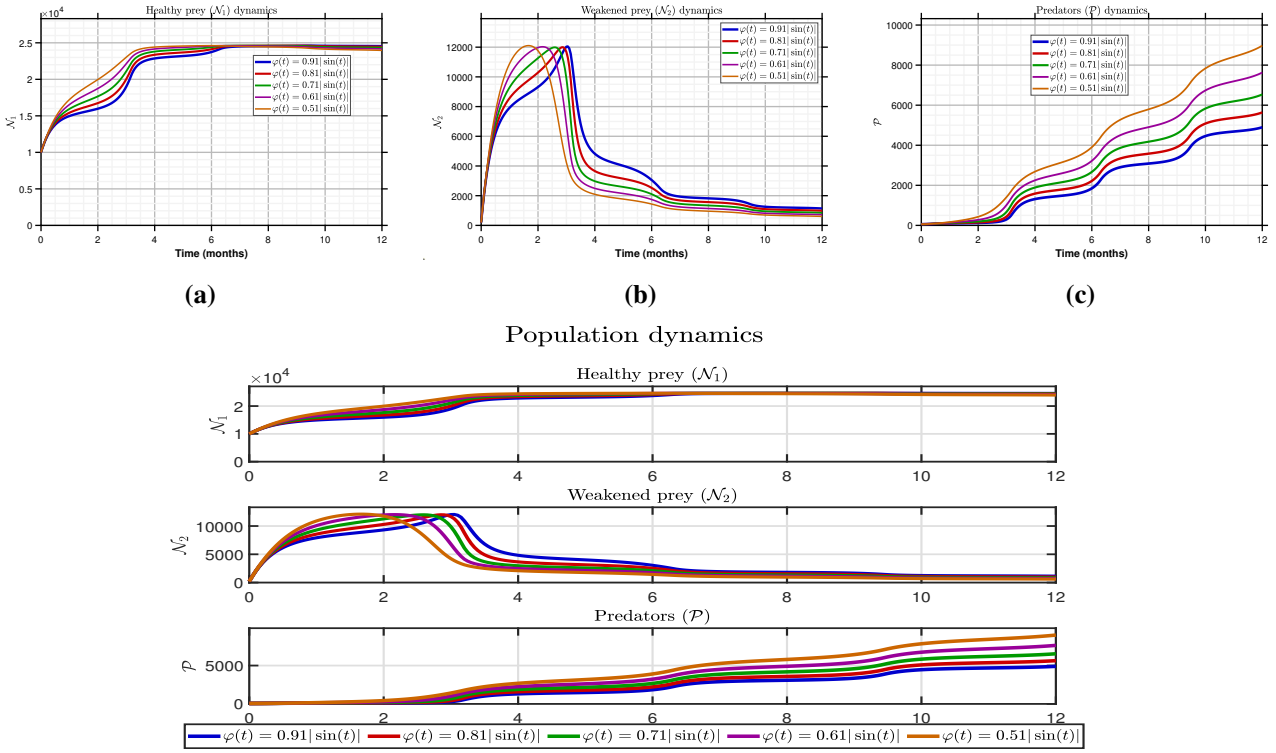

Figure 2. Visualization of $\mathcal{N}_1$, $\mathcal{N}_2$, and $\mathcal{P}$ for fixed $\gamma = 0.1$.

Table 2 shows the final state values of the populations $\mathcal{N}_1$, $\mathcal{N}_2$, and $\mathcal{P}$ at time $t = 12$, computed for a fixed value of the parameter $\gamma = 0.1$ across different fractional orders $\varphi(t)$.

Table 2. Population dynamics with varying fractional orders $\varphi(t)$ at $t = 12$ months.

$\varphi(t)$	$\mathcal{N}_1$ final	$\mathcal{N}_2$ final	$\mathcal{P}$ final
$\varphi(t) = 0.91\|\sin(t)\|$	24,553	1139	4898
$\varphi(t) = 0.81\|\sin(t)\|$	24,461	984	5639
$\varphi(t) = 0.71\|\sin(t)\|$	24,333	844	6536
$\varphi(t) = 0.61\|\sin(t)\|$	24,167	718	7631
$\varphi(t) = 0.51\|\sin(t)\|$	23,390	605	8974

Figure 3 presents the population dynamics of $\mathcal{N}_1$, $\mathcal{N}_2$, and $\mathcal{P}$ for fixed drought parameter $\gamma = 0.2$ and varying fractional order $\varphi(t)$. The drastic decline in healthy prey population from 24,533 for $\gamma = 0.1$ to 2826 for $\gamma = 0.2$ points toward a threshold beyond which drought stress dominates the reproductive potential of the prey population. This corresponds to the ecological concept of a tipping point, beyond which an ecosystem state shifts dramatically.

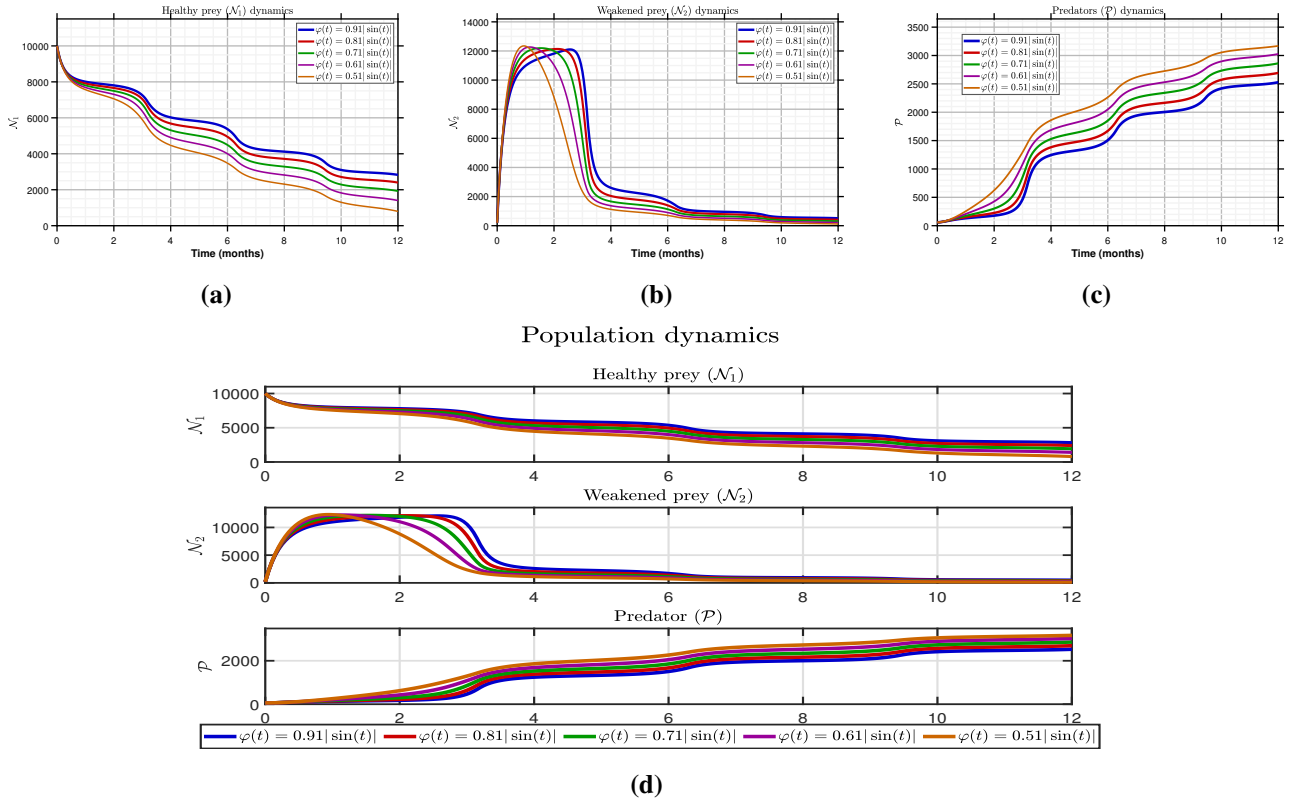

Figure 3. Visualization of $\mathcal{N}_1$, $\mathcal{N}_2$, and $\mathcal{P}$ for fixed $\gamma = 0.2$.

Table 3 lists the final population values of $\mathcal{N}_1$, $\mathcal{N}_2$, and $\mathcal{P}$ at $t = 12$ for a fixed drought parameter $\gamma = 0.2$ and different variable orders $\varphi(t)$.

Table 3. Population dynamics with varying fractional order $\varphi(t)$ at $t = 12$ months.

$\varphi(t)$	$\mathcal{N}_1$ final	$\mathcal{N}_2$ final	$\mathcal{P}$ final
$\varphi(t) = 0.91\|\sin(t)\|$	2826	512	2529
$\varphi(t) = 0.81\|\sin(t)\|$	2397	407	2694
$\varphi(t) = 0.71\|\sin(t)\|$	1925	308	2862
$\varphi(t) = 0.61\|\sin(t)\|$	1398	212	3026
$\varphi(t) = 0.51\|\sin(t)\|$	794	117	3169

A comparison of population dynamics for $\mathcal{N}_1$, $\mathcal{N}_2$, and $\mathcal{P}$ is provided in Figure 4 for $\gamma = 0.1$. The computed values for $\mathcal{N}_1$, $\mathcal{N}_2$, and $\mathcal{P}$ at $t = 12$ are 24, 048, 649, and 8403, respectively. Based on the population levels obtained for $\mathcal{N}_1$, $\mathcal{N}_2$, and $\mathcal{P}$, it is evident that in this case, where memory is incorporated in the system, the population of the prey $\mathcal{N}_1$ is high, and that of the alternative prey $\mathcal{N}_2$ is

low, whereas the predator population $\mathcal{P}$ is moderate. This suggests that even with VO memory effects, the system stabilizes at a configuration where one prey species dominates, consistent with competitive exclusion principles modulated by predator pressure.

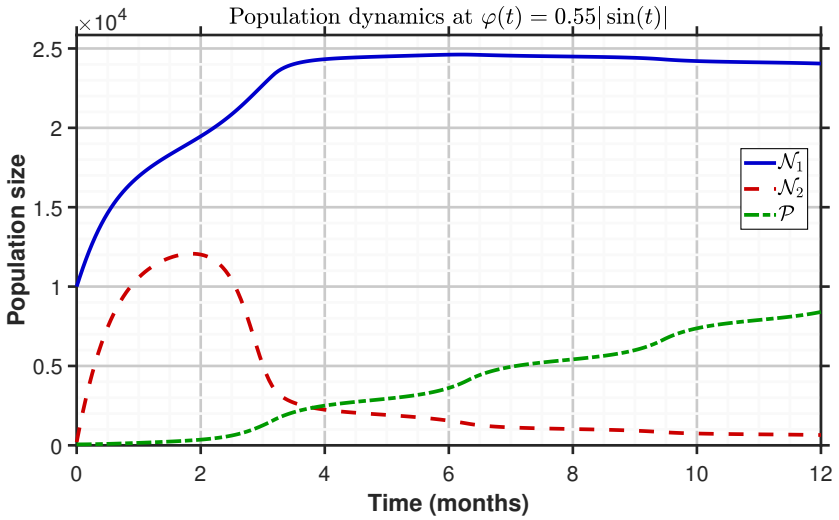

Figure 4. Comparison of $\mathcal{N}_1$, $\mathcal{N}_2$, and $\mathcal{P}$ for fixed $\gamma = 0.1$.

Figure 5 illustrates a comparison of the population dynamics for species $\mathcal{N}_1$, $\mathcal{N}_2$, and $\mathcal{P}$ when $\gamma = 0.2$. We observe that the final populations for all three species are $\mathcal{N}_1 = 1047$, $\mathcal{N}_2 = 155$, and $\mathcal{P} = 3116$ when $t = 12$. A sharp decline in the final populations for all three species is evident when compared to the $\gamma = 0.1$ case, in which the final populations for the three species are $\mathcal{N}_1 = 24048$, $\mathcal{N}_2 = 649$, and $\mathcal{P} = 8403$. This demonstrates the high sensitivity of all three species to drought intensity.

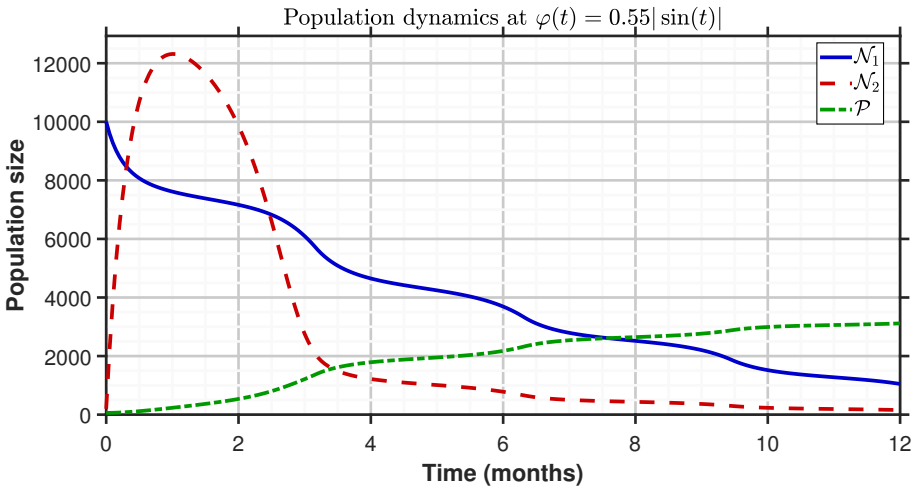

Figure 5. Comparison of $\mathcal{N}_1$, $\mathcal{N}_2$, and $\mathcal{P}$ for fixed $\gamma = 0.2$.

Three-dimensional phase portraits and projections of the system for $\gamma = 0.2$ and various fractional orders $\varphi(t)$ are shown in Figure 6. Overlapping trajectories imply that the qualitative nature of the system is invariant for the chosen values of parameters, whereas quantitative changes are evident.

Biologically, this suggests that the predator–prey dynamics are robust to changes in how strongly past conditions influence the present. A stable ecosystem is maintained across all regimes.

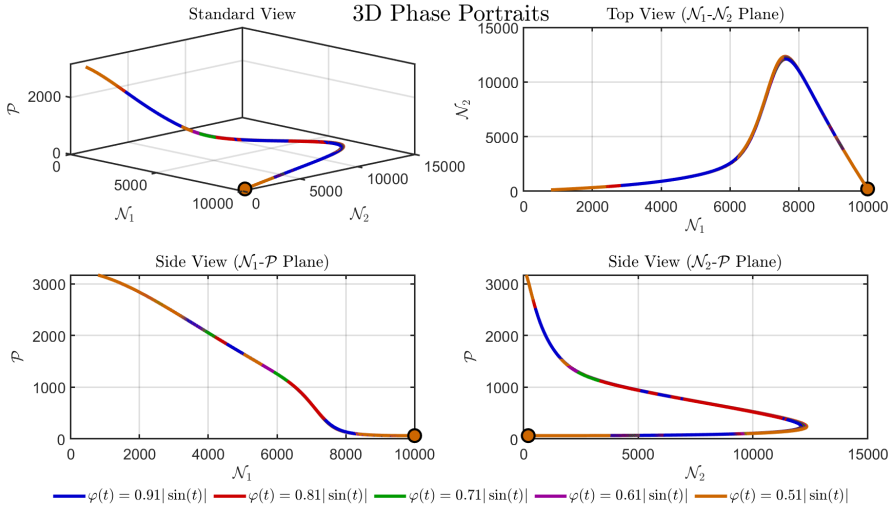

Figure 6. Phase portrait and side view of $\mathcal{N}_1$, $\mathcal{N}_2$ and $\mathcal{P}$ at $\gamma = 0.2$.

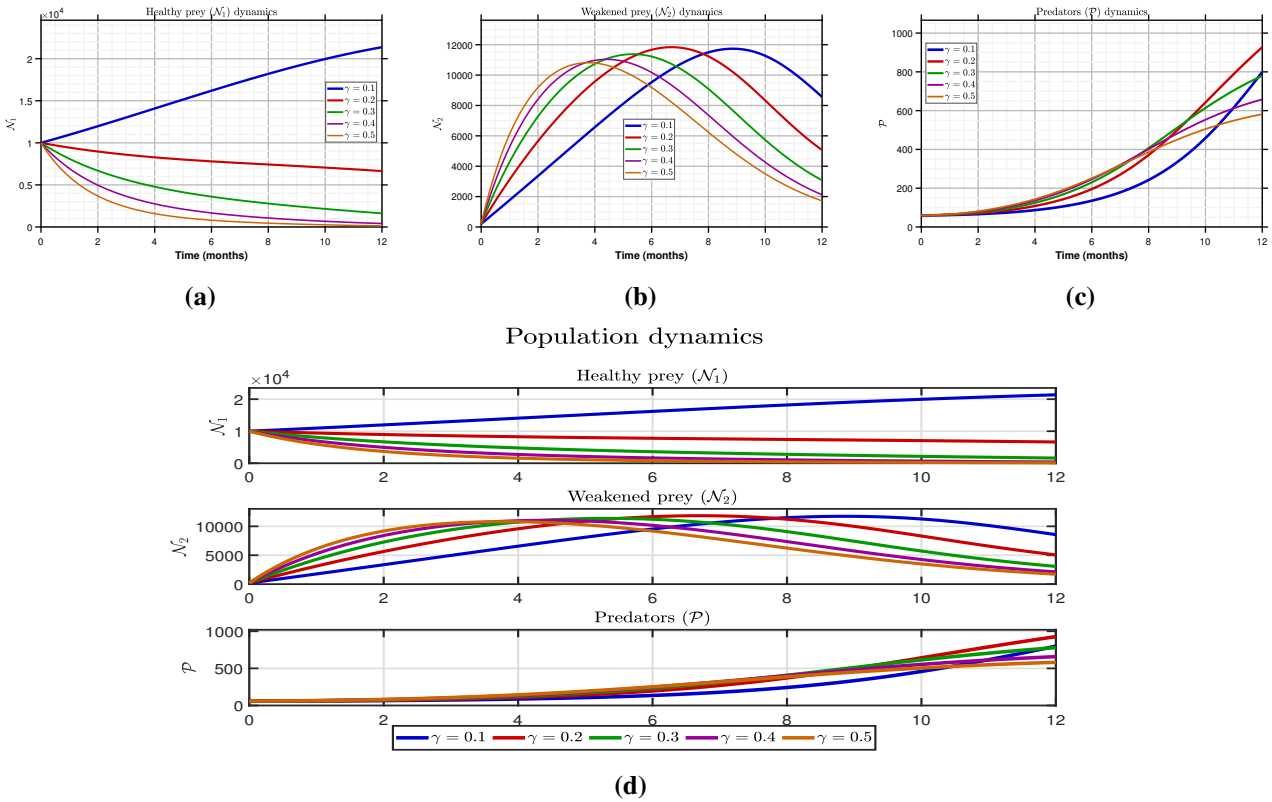

Figure 7. Visualization of $\mathcal{N}_1$, $\mathcal{N}_2$, and $\mathcal{P}$ for fixed $\varphi(t) = 0.85|sint|$.

The population dynamics of $\mathcal{N}_1$, $\mathcal{N}_2$, and $\mathcal{P}$ for a fixed VO $\varphi(t) = 0.85|\sin t|$ and varying γ are shown in Figure 7. As γ increases from 0.1 to 0.5, $\mathcal{N}_1$ undergoes a catastrophic decline, plummeting

from 21,369 to a mere 133. Conversely, the alternative prey $\mathcal{N}_2$, although also declining, becomes the relatively more abundant prey species at higher drought levels ($\gamma \geq 0.3$). This indicates a possible reversal of competitive dominance under extreme resource limitation. Under more favorable conditions, $\mathcal{N}_2$, being more drought-resistant, is outcompeted by $\mathcal{N}_1$. The predator $\mathcal{P}$ remains stable but could be changing its diet from $\mathcal{N}_1$, which is now scarce, to $\mathcal{N}_2$, which is more robust. This analysis shows that γ, the drought parameter, is not merely a scaling factor but rather plays a significant role in determining species interactions.

Numerical results for the populations $\mathcal{N}_1$, $\mathcal{N}_2$, and $\mathcal{P}$ at $t = 12$ are given in Table 4. These values are computed for the fractional order $\varphi(t) = 0.85|\sin t|$ across a range of drought parameters γ.

Table 4. Final population values with fixed $\varphi(t) = 0.85$ at $t = 12$ months.

γ	$\mathcal{N}_1$ final	$\mathcal{N}_2$ final	$\mathcal{P}$ final
0.10	21,369	8563	799
0.20	6643	5063	927
0.30	1621	3070	780
0.40	407	2119	658
0.50	133	1717	582

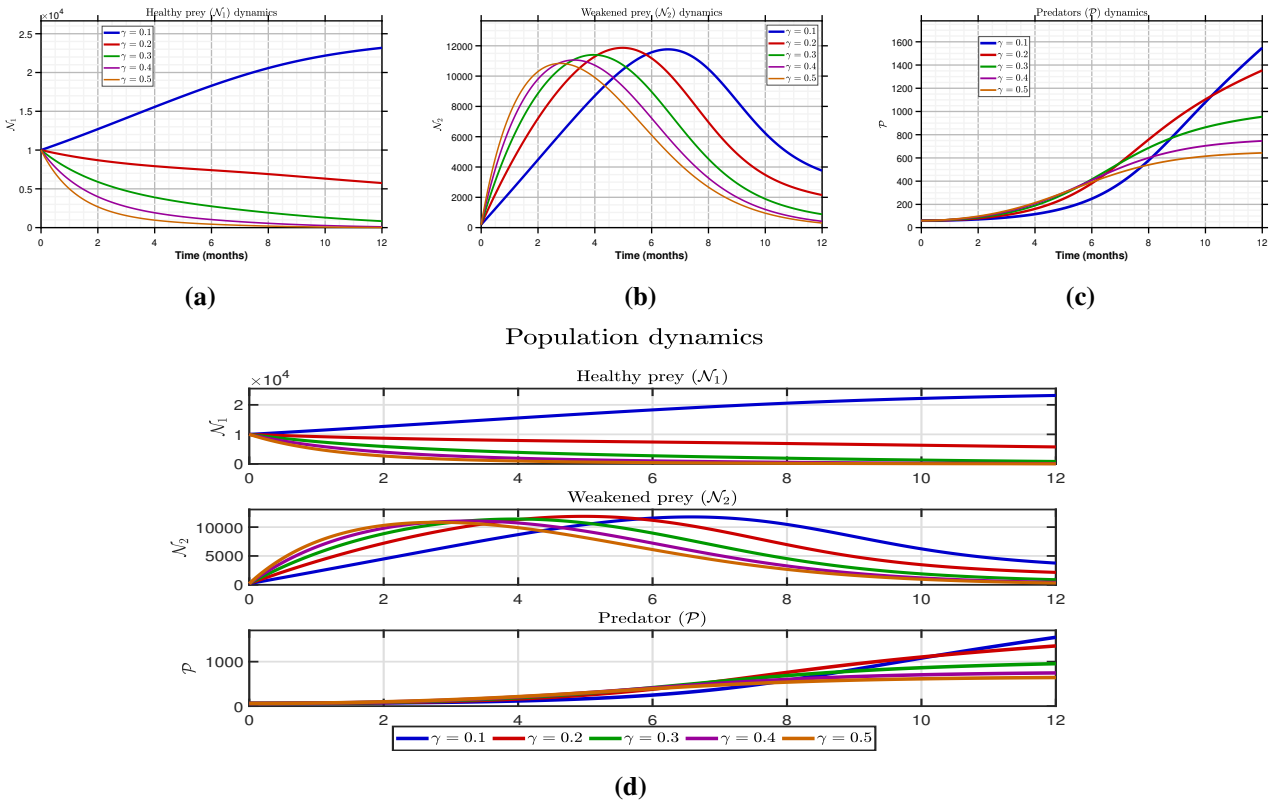

Figure 8. Visualization of $\mathcal{N}_1$, $\mathcal{N}_2$, and $\mathcal{P}$ for fixed $\varphi(t) = 0.75|sint|$.

Figure 8 displays the population dynamics of $\mathcal{N}_1$, $\mathcal{N}_2$, and $\mathcal{P}$ for a fixed fractional order $\varphi(t) = 0.75|\sin t|$ and for various values of γ. A comparison with Figure 7 indicates that the dynamics are

affected significantly by the fractional order $\varphi(t)$. There are two main biological differences. First, for $\gamma = 0.1$, the dominance of $\mathcal{N}_1$ is higher in the case of $\varphi(t) = 0.75|sint|$ (23, 183 vs. 3759) compared to $\varphi(t) = 0.85|sint|$ (21, 369 vs. 8563), showing that stronger memory makes a stronger impact on the competitive advantage of $\mathcal{N}_1$ in the presence of abundant resources. Second, the onset of competitive reversal is delayed in the case of stronger memory. For $\gamma = 0.3$, $\mathcal{N}_1$ and $\mathcal{N}_2$ are comparable in the case of $\varphi(t) = 0.75|sint|$ (830 vs. 880), whereas in the case of $\varphi(t) = 0.85|sint|$, $\mathcal{N}_2$ is dominant (1621 vs. 3070). Thus, stronger memory delays the onset of drought effects and makes $\mathcal{N}_1$ less susceptible to drought. For $\gamma \geq 0.4$, $\mathcal{N}_1$ declines to critically low levels regardless of memory strength.

Table 5 shows the final values of $\mathcal{N}_1$, $\mathcal{N}_2$, and $\mathcal{P}$ at $t = 12$ for $\varphi(t) = 0.75|\sin t|$ under different γ. These results complement those in Table 4, illustrating the effect of reducing the fractional order.

Table 5. Final population values with fixed fractional order $\varphi(t) = 0.75$ at $t = 12$ months.

γ	$\mathcal{N}_1$ final	$\mathcal{N}_2$ final	$\mathcal{P}$ final
0.10	23,183	3759	1548
0.20	5745	2150	1354
0.30	830	880	955
0.40	104	416	747
0.50	13	303	643

Phase portraits illustrating the dynamics of $\mathcal{N}_1$, $\mathcal{N}_2$, and $\mathcal{P}$ under fixed VO memory and varying drought intensities are shown in Figures 9–14. Across all memory regimes, the geometry of the trajectories remains consistent for a fixed $\varphi(t)$, suggesting that the qualitative ecological structure is independent of drought intensity. Instead, only the quantitative scale, specifically population sizes, contracts as drought intensifies. Consequently, the system exhibits structural resilience to environmental changes.

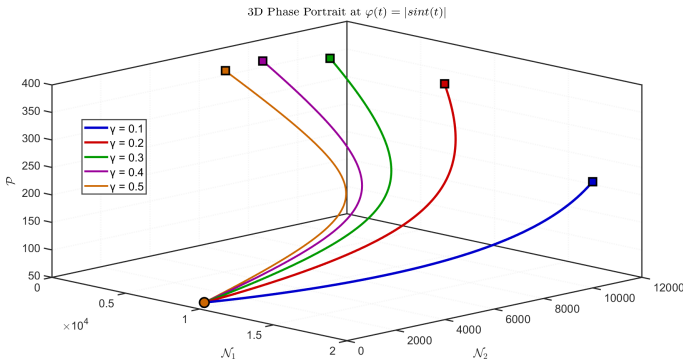

Figure 9. Phase portrait of $\mathcal{N}_1$, $\mathcal{N}_2$, and $\mathcal{P}$ at $\varphi(t) = |sint|$.

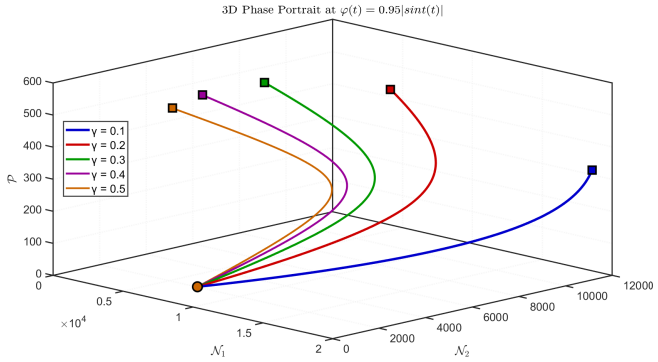

Figure 10. Phase portrait of $\mathcal{N}_1$, $\mathcal{N}_2$, and $\mathcal{P}$ at $\varphi(t) = 0.95|sint|$.

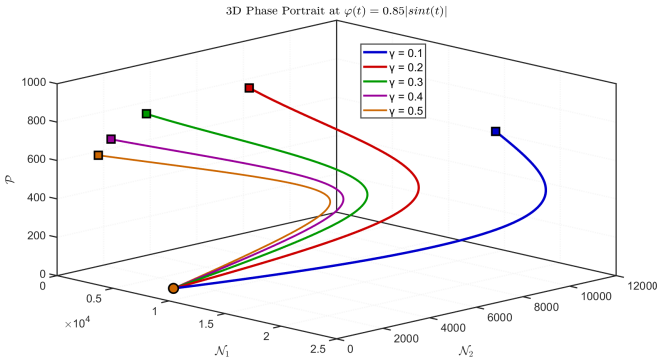

Figure 11. Phase portrait of $\mathcal{N}_1$, $\mathcal{N}_2$, and $\mathcal{P}$ at $\varphi(t) = 0.85|sint|$.

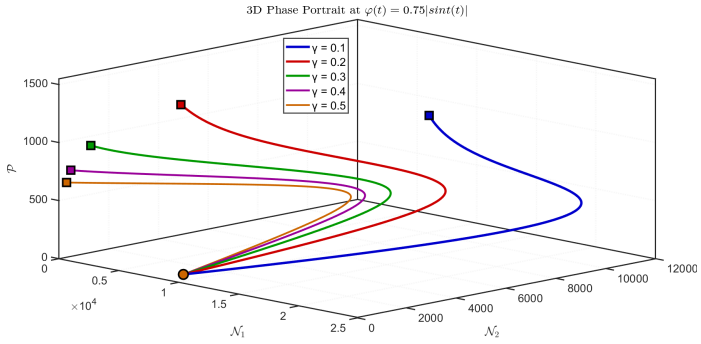

Figure 12. Phase portrait of $\mathcal{N}_1$, $\mathcal{N}_2$, and $\mathcal{P}$ at $\varphi(t) = 0.75|sint|$.

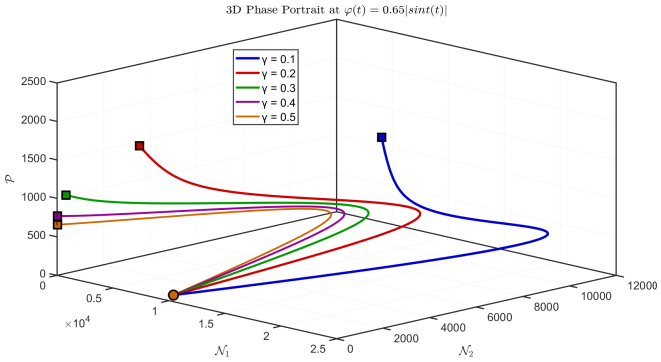

Figure 13. Phase portrait of $\mathcal{N}_1$, $\mathcal{N}_2$, and $\mathcal{P}$ at $\varphi(t) = 0.65|sint|$.

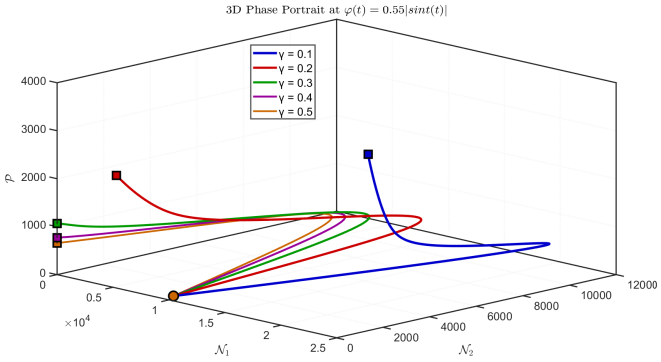

Figure 14. Phase portrait of $\mathcal{N}_1$, $\mathcal{N}_2$, and $\mathcal{P}$ at $\varphi(t) = 0.55|sint|$.

5.3. Comparing variable and constant order dynamics

In integer-order models, stability at equilibrium points remains constant over time. However, in the proposed VO model, as $\varphi(t)$ varies between 0.5 and 1.0, local stability features change seasonally. This is more realistic for ecological systems because populations often exhibit prolonged stable periods interspersed with sudden fluctuations. In classical models, memory loss decays at a constant rate across all time points; in contrast, in the proposed VO model, memory loss varies seasonally according to $\varphi(t)$. During dry seasons, more memory of past droughts is retained in the system, whereas during wet seasons, memory loss occurs more rapidly. This provides a more realistic ecological system where drought legacy effects vary seasonally. Furthermore, in the proposed VO model, the attractor evolves gradually over time, whereas in classical models, the attractors are static. This offers a more realistic representation of ecological systems, where slow regime shifts are more likely to occur in ecosystems rather than a system making a jump to a new state of stability.

6. Neural network methodology and results

We develop a feedforward NN as a surrogate modelling framework for the VO predator–prey system (2.2). The network serves two complementary purposes. First, it provides an independent validation of the numerical scheme (5.7) by learning the underlying solution operator. Second, it enables rapid

prediction of population dynamics for real-time ecological applications once trained.

Training data is generated by numerically simulating the VO system using the scheme (5.7) with parameters in Table 1 and $\gamma = 0.17$ over 240 time steps ($\Delta t = 0.05$). This yields a dataset of 240 samples, each consisting of five input features and three output targets.

At each time step t_n, the five input features are as follows

- $\mathcal{N}_1(t_n)$: current healthy prey population
- $\mathcal{N}_2(t_n)$: current weakened prey population
- $\mathcal{P}(t_n)$: current predator population
- t_n: current time
- $\varphi(t_n) = |\sin(t_n)|$: current fractional order

The corresponding three output targets are the populations at the next time step:

$$\mathbf{y}_n = [\mathcal{N}_1(t_{n+1}),\ \mathcal{N}_2(t_{n+1}),\ \mathcal{P}(t_{n+1})]^T.$$

All input and output data are normalized to the range $[0, 1]$ to enhance training stability and convergence.

The architecture of the implemented NN was 5-30-25-3. It has five neurons in the input layer corresponding to the dimensions of the input features. It then has a first hidden layer of 30 neurons with sigmoid activation, followed by a second hidden layer of 25 neurons also with sigmoid activation. Finally, it has an output layer of three neurons with linear activation. The training algorithm used is Levenberg–Marquardt. The dataset is divided into 70% training (168 samples), 15% validation (36 samples), and 15% testing (36 samples). The performance metric is mean squared error (MSE). The training parameters are a maximum of 1000 epochs, a performance goal of 1×10^{-6}, and a maximum of 20 validation failures.

Convergence for the NN took place exceptionally in the 10th epoch. The final training MSE, validation MSE, and test MSE for the model are 9.19×10^{-7}, 9.32×10^{-7}, and 6.70×10^{-7}, respectively. Figure 15 presents the detailed training analysis of the 5-30-25-3 feedforward NN. In the left panel of the figure, the performance history is presented. It is shown that the training of the three datasets is finished within 10 epochs. Moreover, the convergence of the three data sets is very fast. In the middle panel of the figure, the final values of the MSE for the three data sets are presented. It is shown that the test data set results in the minimum value of the error. The dataset distribution on the right panel illustrates the 70%–15%–15% split strategy employed.

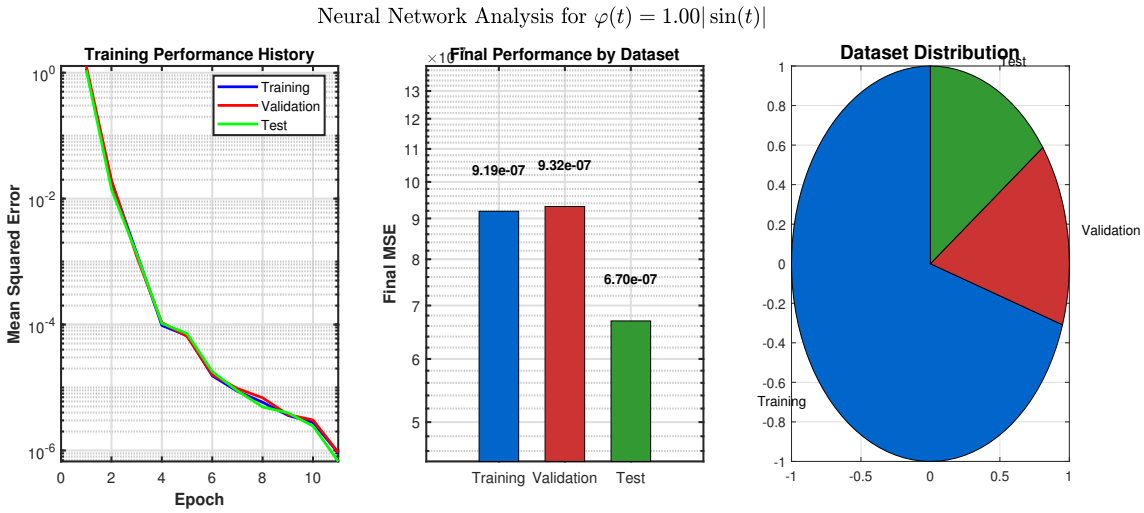

Figure 15. Training performance metrics at $\varphi(t) = |\sin(t)|$.

We show a detailed visualization of the predictive performance of the NN in Figure 16. The first column shows the close agreement of numerical solutions and NN prediction for $\mathcal{N}_1$, $\mathcal{N}_2$, and $\mathcal{P}$. The second column shows that the prediction errors remain consistently low throughout the simulation. The third column shows that the error is distributed symmetrically significantly around zero.

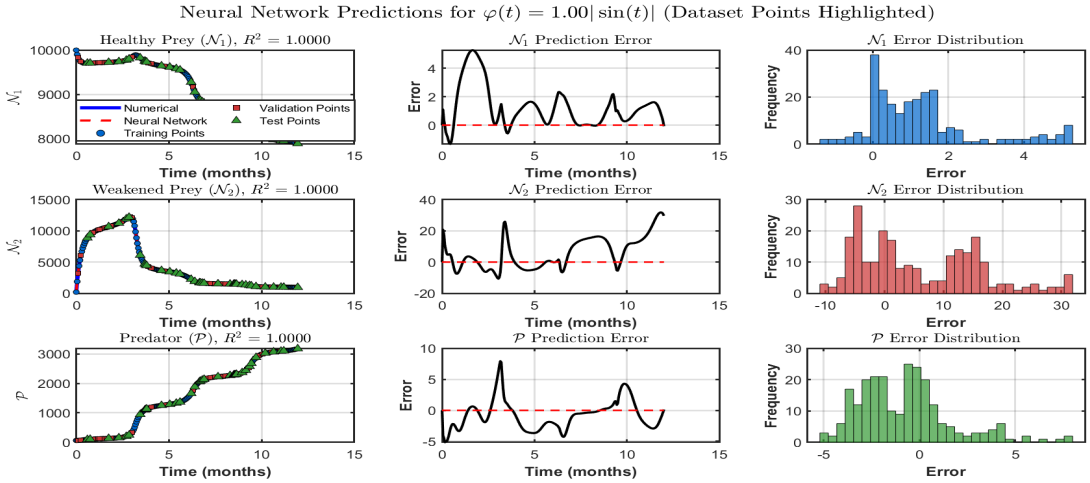

Figure 16. Temporal error, predictions error, and error distributions for $\mathcal{N}_1$, $\mathcal{N}_2$, and $\mathcal{P}$.

The NN's performance remains consistent in various data splits in Figure 17. In the first column, the plots of RMSE have shown that the level of error remains constant. Population $\mathcal{N}_1$ has shown the optimal result with a slight increase in population $\mathcal{N}_2$. In the second column, it can be seen that accuracy is perfect because R^2 is shown. In the third column, the histograms show symmetric error distributions near zero.

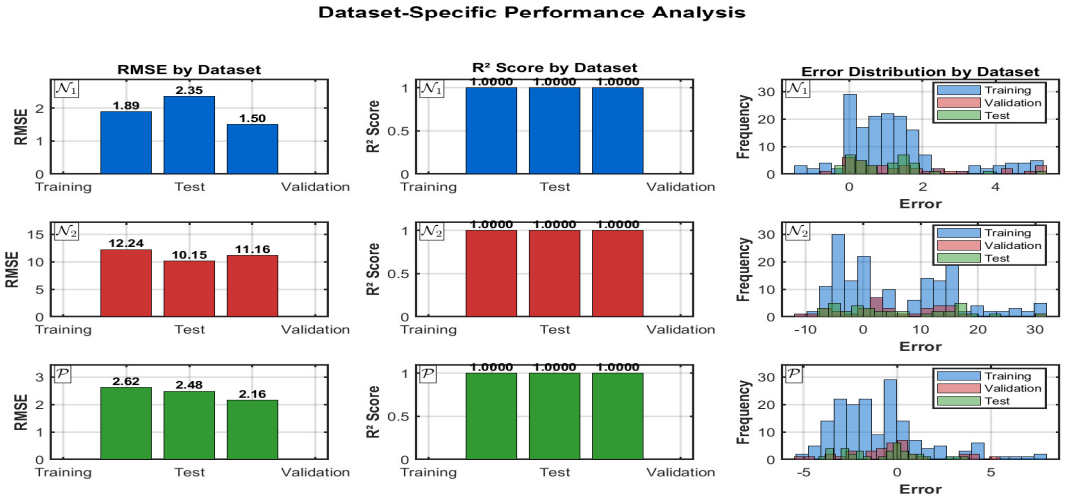

Figure 17. RMSE, R^2, and error distributions for $\mathcal{N}_1$, $\mathcal{N}_2$, and $\mathcal{P}$.

Figure 18 illustrates the regression analysis of the NN predictions and the truth values. The subplot represents the prediction and actual values for the population values. Points on the diagonal indicate perfect prediction. The clustering of all points on the diagonal for all populations in all datasets indicates perfect prediction accuracy. The overall performance across all dataset partitions indicates the overall generalization ability of the network and the absence of overfitting.

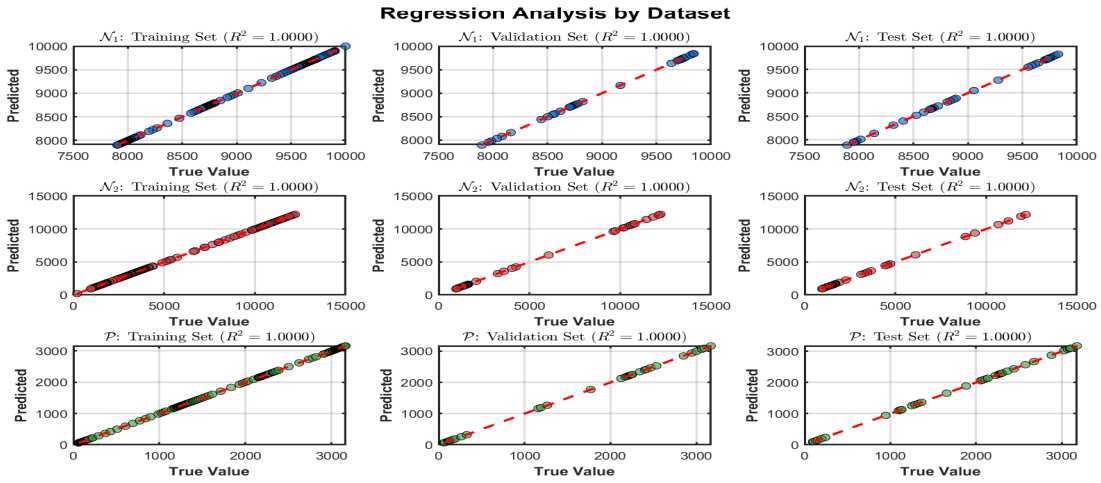

Figure 18. Regression plots of NN predictions against true values of $\mathcal{N}_1$, $\mathcal{N}_2$, and $\mathcal{P}$.

The summary of the detailed error analysis of the NN predictions is shown in Figure 19. The left panel of Figure 19 provides a comparison of all populations in terms of various error measures, which indicates that $\mathcal{N}_1$ has the lowest absolute errors, whereas $\mathcal{N}_2$ has relatively larger absolute errors but still retains high relative accuracy. The central panel of Figure 19 confirms that all populations have perfect R^2 scores of 1, which signifies a perfect linear correlation between the prediction and actual values. The right panel of Figure 19 represents a comparison of the distribution of the magnitude of the error to the size of the population, which indicates that all predictions are accurate to a level of

1% of the population magnitude. The performance across the different dataset splits is summarized in Table 6.

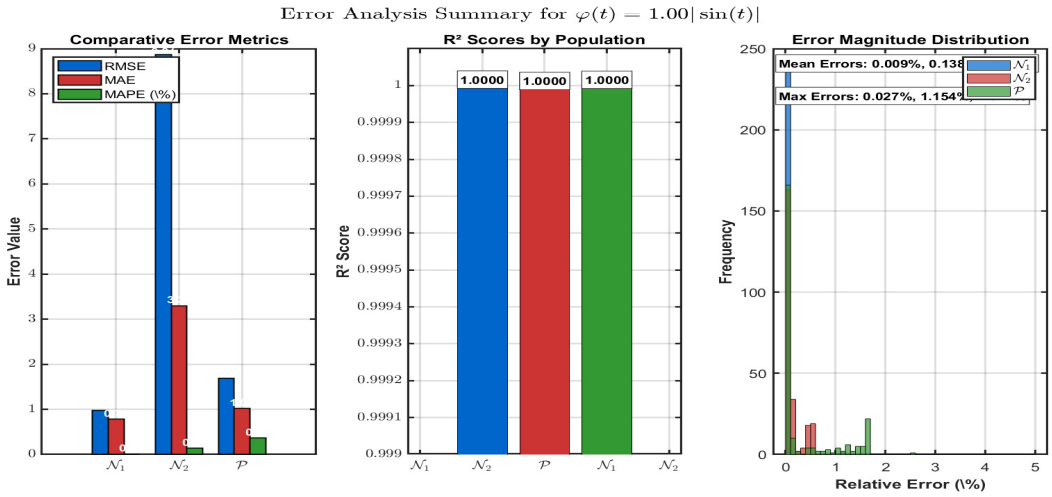

Figure 19. Summary of prediction errors for all three populations.

Table 6. Dataset-specific performance metrics.

Dataset	Samples	Avg RMSE	Avg R^2	Purpose
Training	168	5.5819	1	Network training
Validation	36	4.9941	1	Hyperparameter tuning
Testing	36	4.9388	1	Unseen data evaluation

The NN presented a significant predictive accuracy for all three populations, as detailed in Table 7.

Table 7. Overall prediction performance metrics.

Metric	$\mathcal{N}_1$	$\mathcal{N}_2$	$\mathcal{P}$
RMSE	1.9114	11.7640	2.5277
MAE	1.3395	8.9323	2.0011
MAPE (%)	0.0145	0.5863	0.5929
R^2 Score	1	1	1

The combination of NNs and finite difference has several synergistic benefits, which cannot be achieved by either of these tools alone:

- The numerical method provides numerical approximations, and it is difficult to validate these approximations for VO systems of nonlinear equations because exact analytical solutions are not obtainable. The NN model, by providing its own set of approximate solutions, validates our numerical method. If both models provide similar results, then our numerical method is validated.
- Once the NN is trained, it takes only milliseconds to obtain approximate solutions for different sets of parameters, whereas numerical methods take minutes. This enables rapid exploration of parameter space and real time scenario analysis.

- The numerical method may not only introduce numerical noise in the results, especially near sharp transitions, but the NN model, by learning the underlying functional relationship, automatically removes this noise from the results.
- In our numerical method, it is necessary to compute the convolution weights at every time step because the VO function $\varphi(t)$ is involved. However, after training the NN model on these computations, it automatically captures the order effects without having to recalculate historical dependencies.
- Ensemble NNs can provide prediction intervals and uncertainty estimates, which are difficult to obtain from deterministic finite difference methods alone.

This hybrid method combines the mathematical precision and interpretability of the finite difference scheme with the computational efficiency, generality, and uncertainty quantification of NNs.

7. Scalability and robustness analysis

A detailed analysis of the scalability and robustness of our method is performed. Several factors influence the scalability and practical application of our NN-enhanced method to real-world ecological data.

7.1. Robustness to sparse data

Real-world ecological data sets often suffer from irregular and sparse sampling. We tested our method by gradually reducing the amount of available data from 100% down to 5% of the original 241 time points and measured the prediction accuracy by using interpolation as a reference method. As illustrated in Table 8, the prediction error gradually increases with decreasing data availability. Although the average RMSE of all three populations at 50% (121 points), or half of the original time points, is 23.1, which represents a slight increase in prediction error, the average RMSE remains at 102.8 even at 20% (48 points) data availability. However, at 10% (24 points) and lower, the prediction error increases significantly, with RMSE values of 354.4 and 646.6 at 10% and 5% data availability, respectively. These results imply that our method requires at least 20% of the total time points (48 points) in the time series for reliable prediction.

Table 8. RMSE under varying data availability.

Data available	Samples	$\mathcal{N}_1$	$\mathcal{N}_2$	$\mathcal{P}$	Average
100%	241	0.0	0.0	0.0	0.0
50%	121	2.3	61.4	5.6	23.1
30%	72	8.7	95.2	6.8	36.9
20%	48	20.8	264.0	23.6	102.8
10%	24	32.6	1006.1	24.5	354.4
5%	12	83.7	1696.5	159.6	646.6

7.2. Robustness to measurement noise

We evaluated the resilience of the method to noise by adding Gaussian noise at levels ranging from 0% to 30% of the signal magnitude, followed by a simple moving average filter (window size 5) for

denoising. Table 9 quantifies the denoising robustness. Average RMSE increases from 42.3 at 0% noise to 146.2 at 5%, 264.0 at 10%, and 380.8 at 15%. Beyond 15%, error escalates rapidly, reaching 558.5 at 20% and 700.5 at 30% noise. The method remains effective up to 15% noise.

Table 9. Denoising performance across noise levels (RMSE).

Noise level	$\mathcal{N}_1$	$\mathcal{N}_2$	$\mathcal{P}$	Average
0%	6.5	117.3	3.2	42.3
5%	212.9	183.4	42.3	146.2
10%	407.4	296.5	88.1	264.0
15%	635.7	380.1	126.7	380.8
20%	916.3	591.9	167.3	558.5
30%	1265.4	584.1	252.1	700.5

7.3. Computational scalability

We assessed the computational requirements of both the proposed VO model and the NN enhanced scheme across varying data sizes from 100 to 5000 points. Table 10 summarizes the computational scaling. Simulation time remains efficient throughout, requiring only 0.0082 seconds for 5000 data points. The NN prediction time, estimated at 0.05 ms per time step, demonstrates real-time capability with 250 ms required for predicting all 5000 points. Memory requirements remain negligible at 0.24 MB for the largest dataset. These results confirm that the proposed scheme is highly scalable and suitable.

Table 10. Computational scaling with data size.

Data points	Simulation time (s)	NN prediction (s)	Total time (s)	Memory (MB)
100	0.0079	0.0050	0.0129	0.00
500	0.0005	0.0250	0.0255	0.02
1000	0.0006	0.0500	0.0506	0.05
2000	0.0017	0.1000	0.1017	0.10
5000	0.0082	0.2500	0.2582	0.24

7.4. Neural network training requirements

A major factor in NN-based approaches is the amount of training data required. According to established guidelines, given the architecture and the number of parameters, which is 1033 in our case, a minimum of 5–10 times more data samples should be considered for efficient training of the model, that is, 5165–10,330 data samples. In our case, our current dataset has 240 input–output pairs of data from our 12-month simulation period with 0.05-month time steps. Our results demonstrate that the network successfully captures the essential dynamics with this limited dataset.

8. Conclusions

In this research, a mathematical framework for analyzing drought-stressed predator–prey interactions using VO fractional calculus has been established. The well-posedness and UH stability of

the proposed mathematical model have been verified by theoretical analysis. A finite difference method has been presented, coupled with the NN approach for numerical validation. This framework has important ecological significance, as predator–prey interactions under drought stress have important ecological implications. The determination of a critical drought stress level, near $\gamma = 0.3$, offers quantitative management strategies for drought-stressed ecosystems. The VO fractional-order analysis shows that memory, represented by $\varphi(t)$, plays a significant role in ecosystem resilience, as more memory leads to greater predator survival but longer recovery times. The VO analysis is unique compared to classical models analysis, as it includes time-dependent adaptability of real-world ecosystems under changing environmental conditions. The novelty of the research lies in the integrated methodology for analyzing nonlinear predator–prey interactions. The proposed NN scheme demonstrates exceptional accuracy for predicting nonlinear predator-prey interactions and has validated the proposed numerical scheme. Despite these advantages, there are several limitations to the proposed mathematical framework. The ecological model assumes spatial homogeneity and relies on literature-based parameters, and the NN component requires sufficient training data for accurate predictions. Future work should address these constraints. This study provides a mathematically sound foundation for understanding drought-induced population shifts and offers practical tools for ecological forecasting under climate change.

Author contributions

Nouf Abdulrahman Alqahtani: Conceptualization, methodology, validation, formal analysis, writing–review and editing, funding acquisition; Mohammadi Begum Jeelani: Conceptualization, software, validation, writing–original draft preparation. All authors have read and agreed to the published version of the manuscript.

Use of Generative-AI tools declaration

The authors declare that AI has not been used to create this research work.

Acknowledgments

This work was supported and funded by the deanship of scientific research at Imam Mohammad Ibn Saud Islamic University (IMSIU) (grant number IMSIU-DDRSP2604).

Conflict of interest

The authors declare that they have no conflicts of interest.

References

1. I. Ahmad, Z. Ali, B. Khan, K. Shah, T. Abdeljawad, Exploring the dynamics of Gumboro-Salmonella co-infection with fractal fractional analysis, *Alex. Eng. J.*, **117** (2025), 472–489. https://doi.org/10.1016/j.aej.2024.12.119

2. H. Alrabaiah, I. Ahmad, R. Amin, K. Shah, A numerical method for fractional variable order pantograph differential equations based on Haar wavelet, *Eng. Comput.*, **38** (2022), 2655–2668. http://doi.org/10.1007/s00366-020-01227-0

3. X. Q. Kong, R. Z. Yang, Dynamics analysis of a Filippov Lymantria dispar-Great tit model with double Allee effects and two-thresholds control, *Math. Comput. Simulat.*, **246** (2026), 25–43. https://doi.org/10.1016/j.matcom.2026.01.028

4. Y. X. Ma, R. Z. Yang, Bifurcation analysis in a modified Leslie-Gower with nonlocal competition and Beddington-DeAngelis functional response, *J. Appl. Anal. Comput.*, **15** (2025), 2152–2184. https://doi.org/10.11948/20240415

5. F. Y. Zhu, R. Z. Yang, Bifurcation in a modified Leslie-Gower model with nonlocal competition and fear effect, *Discrete Cont. Dyn.-B*, **30** (2025), 2865–2893. https://doi.org/10.3934/dcdsb.2024195

6. F. T. Wang, R. Z. Yang, X. Zhang, Turing patterns in a predator-prey model with double Allee effect, *Math. Comput. Simulat.*, **220** (2024), 170–191. https://doi.org/10.1016/j.matcom.2024.01.015

7. R. Z. Yang, F. T. Wang, D. Jin, Spatially inhomogeneous bifurcating periodic solutions induced by nonlocal competition in a predator–prey system with additional food, *Math. Method. Appl. Sci.*, **45** (2022), 9967–9978. https://doi.org/10.1002/mma.8349

8. W. J. Li, L. T. Zhang, J. D. Cao, A note on Turing–Hopf bifurcation in a diffusive Leslie–Gower model with weak Allee effect on prey and fear effect on predator, *Appl. Math. Lett.*, **172** (2026), 109741. https://doi.org/10.1016/j.aml.2025.109741

9. W. J. Li, L. A. Yang, L. H. Huang, J. D. Cao, Threshold dynamics analysis of a diffusive dengue disease transmission model, *Commun. Nonlinear Sci.*, **152** (2025), 109247. https://doi.org/10.1016/j.cnsns.2025.109247

10. W. J. Li, L. T. Zhang, J. D. Cao, F. Xu, Z. W. Cai, Finite time attractivity and exponentially stable of a multi-stage epidemic system with discontinuous incidence, *Qual. Theory Dyn. Syst.*, **24** (2025), 199. http://doi.org/10.1007/s12346-025-01358-z

11. F. A. Rihan, Numerical modeling of fractional-order biological systems, *Abstr. Appl. Anal.*, **2013** (2013), 816803. https://doi.org/10.1155/2013/816803

12. F. A. Rihan, D. Baleanu, S. Lakshmanan, R. Rakkiyappan, On fractional SIRC model with salmonella bacterial infection, *Abstr. Appl. Anal.*, **2014** (2014), 136263. https://doi.org/10.1155/2014/136263

13. Z. J. Zhang, R. Z. Yang, Dynamics analysis of a Filippov ash infectious diseases model with a saturated incidence rate and delayed mortality, *Math. Comput. Simulat.*, **241** (2026), 513–527. https://doi.org/10.1016/j.matcom.2025.09.014

14. P. J. Hanson, J. F. Weltzin, Drought disturbance from climate change: response of United States forests, *Sci. Total Environ.*, **262** (2000), 205–220. https://doi.org/10.1016/S0048-9697(00)00523-4

15. B. Chakraborty, N. Bairagi, Complexity in a prey-predator model with prey refuge and diffusion, *Ecol. Complex.*, **37** (2019), 11–23. https://doi.org/10.1016/j.ecocom.2018.10.004

16. C. Riginos, Climate and the landscape of fear in an African savanna, *J. Anim. Ecol.*, **84** (2015), 124–133. https://doi.org/10.1111/1365-2656.12262

17. A. Morin, S. Chamaillé-Jammes, M. Valeix, Climate effects on prey vulnerability modify expectations of predator responses to short- and long-term climate fluctuations, *Front. Ecol. Evol.*, **8** (2021), 601202. https://doi.org/10.3389/fevo.2020.601202

18. R. Charles, O. D. Makinde, M. Kung'aro, A review of the mathematical models for the impact of seasonal weather variation and infections on prey predator interactions in Serengeti ecosystem, *Open Journal of Ecology*, **12** (2022), 718–732. http://doi.org/10.4236/oje.2022.1211041

19. H. I. Freedman, P. Waltman, Persistence in models of three interacting predator-prey populations, *Math. Biosci.*, **68** (1984), 213–231. https://doi.org/10.1016/0025-5564(84)90032-4

20. T. D. Sagamiko, N. Shaban, C. L. Nahonyo, O. D. Makinde, Optimal control of a threatened wildebeest-lion prey-predator system incorporating a constant prey refuge in the Serengeti ecosystem, *Appl. Comput. Math.*, **4** (2015), 296–312. http://doi.org/10.11648/j.acm.20150404.18

21. K. Sujatha, M. Gunasekaran, Dynamics in a harvested prey-predator model with susceptible-infected-susceptible (SIS) epidemic disease in the prey, *Advances in Applied Mathematical Biosciences*, **7** (2016), 23–31.

22. T. A. S. Obaid, A. K. Hamoud, Predator-prey relationships system, *International Journal of Computer Applications*, **140** (2016), 42–44. http://doi.org/10.5120/ijca2016909310

23. T. Abdeljawad, M. Sher, K. Shah, M. Sarwar, I. Amacha, M. Alqudah, et al., Analysis of a class of fractal hybrid fractional differential equation with application to a biological model, *Sci. Rep.*, **14** (2024), 18937. http://doi.org/10.1038/s41598-024-67158-8

24. K. Shah, T. Abdeljawad, S. S. Aiady, M. Arfan, Study of variable order mathematical model by using algae as bio-fertilizers, *J. Nonlinear Math. Phys.*, **32** (2025), 92. http://doi.org/10.1007/s44198-025-00331-3

25. X. Y. Li, H. X. Li, B. Y. Wu, A new numerical method for variable order fractional functional differential equations, *Appl. Math. Lett.*, **68** (2017), 80–86. https://doi.org/10.1016/j.aml.2017.01.001

26. H. G. Sun, A. L. Chang, Y. Zhang, W. Chen, A review on variable-order fractional differential equations: mathematical foundations, physical models, numerical methods and applications, *Fract. Calc. Appl. Anal.*, **22** (2019), 27–59. http://doi.org/10.1515/fca-2019-0003

AIMS Press